



HAL
open science

Average-based mesh adaptation for hybrid RANS/LES simulation of complex flows

Sajad Mozaffari, Emmanuel Guilmineau, Michel Visonneau, Jeroen Wackers

► **To cite this version:**

Sajad Mozaffari, Emmanuel Guilmineau, Michel Visonneau, Jeroen Wackers. Average-based mesh adaptation for hybrid RANS/LES simulation of complex flows. *Computers and Fluids*, 2022, 232, pp.105202. 10.1016/j.compfluid.2021.105202 . hal-03388256

HAL Id: hal-03388256

<https://hal.science/hal-03388256>

Submitted on 20 Oct 2021

HAL is a multi-disciplinary open access archive for the deposit and dissemination of scientific research documents, whether they are published or not. The documents may come from teaching and research institutions in France or abroad, or from public or private research centers.

L'archive ouverte pluridisciplinaire **HAL**, est destinée au dépôt et à la diffusion de documents scientifiques de niveau recherche, publiés ou non, émanant des établissements d'enseignement et de recherche français ou étrangers, des laboratoires publics ou privés.

Highlights

Average-based mesh adaptation for hybrid RANS/LES simulation of complex flows

Sajad Mozaffari, Emmanuel Guilmineau, Michel Visonneau, Jeroen Wackers

- Adaptive grid refinement is achieved for hybrid RANS/LES simulations.
- Static mesh topologies based on time-averaged refinement criteria help to preserve the turbulence.
- Accurate and efficient simulation of complex realistic cases is confirmed by tests.

Average-based mesh adaptation for hybrid RANS/LES simulation of complex flows

Sajad Mozaffari^{a,*}, Emmanuel Guilmineau^a, Michel Visonneau^a and Jeroen Wackers^a

^aLaboratoire de recherche en Hydrodynamique, Énergétique et Environnement Atmosphérique, CNRS UMR 6598, Ecole Centrale de Nantes, 1 rue de la Noë, B.P. 92101, 44321 Nantes Cedex 03, France

ARTICLE INFO

Keywords:

Adaptive refinement
Hybrid RANS/LES
Averaged refinement criterion
High Reynolds numbers

ABSTRACT

Generating meshes with the right resolution is crucial for hybrid RANS/LES simulations of high Reynolds number flow with complex physical phenomena and geometries. This makes automatic mesh generation through adaptive refinement an interesting option. However, since the behavior of these turbulence models depends on the local grid size, mesh changes in time as a result of adaptive refinement may affect the production and destruction of turbulence. Therefore, grid adaptation with refinement criteria based on time-averaged quantities is proposed here to produce meshes that do not evolve rapidly in time and that are suitable for capturing the unsteady flow at each instant. Two averaging approaches, averaging over the instantaneous flow field, and averaging over the refinement criterion, are tested to simulate a turbulent flow behind a backward-facing step with a Detached Eddy Simulation type turbulence model. Compared to grid adaptation based on instantaneous solutions, the computational cost is reduced, the accuracy of the solutions improves and an adapted mesh which has a generally static topology based on the main flow features is obtained. The investigation of this refinement process for two realistic test cases, a ship and a hybrid delta wing, confirms the reliability of the average-based adaptation and shows that automatic meshing for hybrid RANS/LES simulations of complex flows is possible.

1. Introduction


In numerical fluid dynamics today, detailed and accurate simulations are performed for more and more complex flows. This is both due to industry demand and for the fundamental analysis of complex-flow physics, since behavior like vortex motion and turbulence creation may not occur in the same way in simpler flows. For flows with separations or strong unsteadiness, Reynolds-averaged Navier-Stokes (RANS) simulation of the turbulence may be inaccurate, while Large-Eddy Simulation (LES) is prohibitively expensive for higher Reynolds numbers. Thus, hybrid RANS/LES methods, which blend both turbulence models and apply each where it is best suited, are often the right choice for these simulations (e.g. [16, 30, 31, 35]).

Meshing for hybrid RANS/LES simulations is challenging, since the behavior of the turbulence model depends strongly on the mesh size. In boundary layers where the turbulence is mostly modeled, too fine meshes may incorrectly reduce the modeled turbulence [33]. However, in those regions of the flow where the resolved turbulence is predominant, the mesh must be sufficiently fine to capture the largest energy-carrying turbulent eddies with several cells. This requires locally very fine meshes, which implies using either a uniform fine mesh over most of the flow domain (which is very expensive), or placing the finest cells exactly at the position of the main flow features. Creating such meshes manually is a time-consuming process, which may require several iterations where the mesh is changed each time, based on the results of earlier simulations.

Adaptive grid refinement (AGR) is a natural solution for this problem. With adaptive refinement, the mesh is changed dynamically during a simulation, to adapt it to the requirements of the evolving flow field. AGR today is used frequently and reliably in RANS simulations for different applications, such as aerodynamics [2, 3, 19], free surface capturing [40, 43], reacting flows [10] and in turbo-machinery configurations [9, 38].

Fewer contributions address mesh adaptation for LES or hybrid RANS/LES turbulence models on complex geometries. For LES, several studies have been carried out on complex geometries with two mesh categories of structured [1, 34] and unstructured [4, 6, 13] meshes. The main aim of these papers is to propose grid adaptation methods

*Corresponding author

 sajad.mozaffari@gmail.com (S. Mozaffari); emmanuel.guilmineau@ec-nantes.fr (E. Guilmineau); michel.visonneau@ec-nantes.fr (M. Visonneau); jeroen.wackers@ec-nantes.fr (J. Wackers)
ORCID(s): 0000-0001-6061-4010 (S. Mozaffari); 0000-0003-1676-5326 (M. Visonneau)

and proper error indicators to tackle the issue which arises when the grid-spacing controls both the numerical and the modeling error, since for LES simulations the optimal mesh cannot be obtained based on the error of the numerical scheme only. For hybrid RANS/LES, using adaptive refinement method is at the beginning of the path. However, with the increasing popularity of hybrid RANS/LES turbulence models for complex geometries, to reduce the mesh generation effort and computational cost and also to get the most out of the capabilities of these models, mesh adaptation has received recent attention [21, 26, 46].

Like for LES however, with hybrid RANS/LES turbulence models, any change in the grid properties affects the performance of the model. This issue must be addressed for any adaptive meshing process. Modifications of the cell sizes in time by the adaptive refinement change the smallest scale for the resolved turbulence before and after the adaptation, which perturbs the turbulence. The same process also appears at the interface between two regions of the mesh with different grid resolutions as a result of local mesh refinement. Hybrid RANS/LES models have inherited this issue from LES, where it was detected by Piomelli et al. [28] and Goodfriend et al. [12] while performing simulations in which interfaces between fine and coarse grids were artificially introduced. In addition, to transfer the solution from the original mesh to the adapted one, interpolation is required. However, due to the strong spatial variation of hybrid LES solutions, interpolation errors may be large and may cause the incorrect transfer of resolved turbulence kinetic energy between meshes.

The effect of these mesh changes is illustrated with an example taken from [23], inspired by [12, 28]: a Detached Eddy Simulation (DES) simulation of freely decaying turbulence in a uniform mean flow, where halfway through the domain, the mesh size becomes twice larger (Fig. 1). When the flow passes from the fine to the coarse grid, the resolved turbulence kinetic energy abruptly diminishes since the local grids cannot represent the smallest eddies that are present on the finer mesh. In addition to the sudden perturbation at the coarse/fine interface, a change in the grid size varies the rate of the dissipation of turbulence. A coarser mesh decreases the artificial dissipation term of the turbulence kinetic energy equation in the DES turbulence model. The resulting slower decay of the modeled turbulence partially compensates for the loss of resolved turbulence, but this effect is gradual rather than immediate. Furthermore, the loss of resolved turbulence is never equal to the gain in modeled turbulence and the difference is large enough to affect the total averaged turbulence kinetic energy. Thus, a single change in mesh size causes a lasting perturbation of the turbulence.

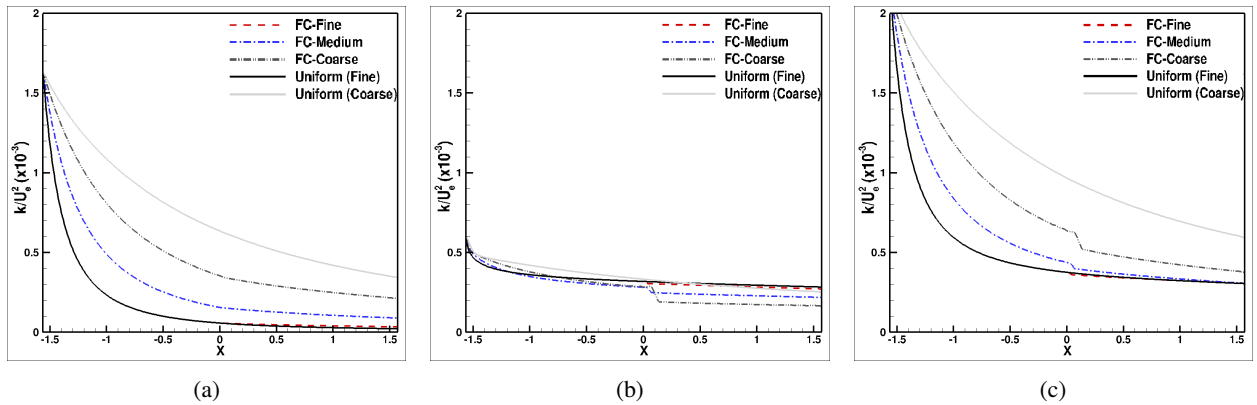


Figure 1: Freely decaying turbulence over a fine-to-course (FC) interface in the mesh at $X = 0$: modeled (a), resolved (b), and total turbulence (c) on three meshes (Fine, Medium, Coarse). The mean flow is left-to-right, the turbulence kinetic energy shown is averaged over the Y - and Z -directions.

For large test cases with complex flow structures, these issues can greatly affect the results and cause unavoidable errors. One may consider these effects as problems with the turbulence modeling, which require improvement. From a mesh designer's perspective however, the conclusion is that any change of the mesh size in space (and by extension, in time) perturbs the turbulence in the flow and should, if possible, be avoided. This has led to mesh adaptation aimed at creating meshes which are nearly constant in time. For LES simulation, Toosi and Larsson [34] proposed anisotropic mesh adaptation based on an error estimator, by considering the equidistribution of the averaged small-scale turbulent energy for each cell, over the cell directions. Daviller et al. [6] defined a metric based on the time-averaged value of the kinetic energy dissipation for unstructured mesh refinement. In the context of p-refinement, an analysis of several

averaged error indicators for discontinuous Galerkin methods was carried out by Naddei et al. [25].

For hybrid RANS/LES simulations, Mozaffari et al. [23, 24] introduced an average-based adaptive mesh refinement which produces a static mesh that can represent the instantaneous flow at any moment. Grid adaptation would normally modify the mesh constantly to follow the turbulent eddies of the flow, but this perturbs the turbulence as seen above. Average-based mesh adaptation can reduce the perturbations instead, by meshing in such a way that each flow feature in a statistically steady flow is propagated on a mesh that is, as much as possible, constant in size.

In this study, the performance and the reliability of the average-based adaptive mesh refinement in combination with hybrid RANS/LES turbulence models is demonstrated for the simulation of complex flows. This work uses the ISIS-CFD incompressible two-fluid Navier-Stokes solver developed by ECN/CNRS, which is introduced in Section 2. Afterwards, a brief description of the average-based AGR method and of the global parameters which affect its performance is provided in Section 3. In a first test (Section 4), the effects of two averaging approaches on the behavior of the adaptation are considered for a backward-facing step (BFS) turbulent flow, using a DES type turbulence model. Changes in the length of the averaging interval and the global mesh fineness are studied as well. The effectiveness of the proposed method, including the recommendations coming from the initial test, is then evaluated for the simulation of two complex, realistic test cases (Section 5): trailing vortices behind a ship and a hybrid delta wing at high angles of attack. Comparisons with reference simulations and experiments serve to test whether the method can reliably simulate such complex flow cases.

2. The flow solver ISIS-CFD

ISIS-CFD is an incompressible unsteady multifluid Navier-Stokes solver, developed by ECN/CNRS [8, 29] and available in the FINETM/Marine suite from NUMECA International. The solver is based on the finite volume method to build the spatial discretization of the transport equations. The discretization is face-based, so cells with an arbitrary number of arbitrarily-shaped faces are accepted; most computations are performed on unstructured hexahedral meshes. Pressure-velocity coupling is obtained through a Rhie & Chow SIMPLE-type method: the velocity field is obtained from the momentum conservation equations and the pressure field is extracted from the continuity equation, transformed into a pressure-equation. Diffusive fluxes are evaluated with central differences, while convective fluxes are either limited in the Normalized Variable Diagram (NVD) [20] or based on an explicit blending of central and second-order upwind reconstructions. The code is fully parallel using the MPI (Message Passing Interface) protocol.

For the Reynolds-averaged Navier-Stokes equations (RANS), the method features the classical two-equation $k - \omega$ SST model, as well as an anisotropic two-equation Explicit Algebraic Reynolds Stress Model (EARS) [8] and Reynolds Stress Transport Models [7], with or without rotation corrections. Hybrid RANS/LES models like DES, DDES (Delayed DES) and IDDES (Improved Delayed DES) based on the $k - \omega$ SST model are also available and have been validated on automotive flows with large separations [16]. Free-surface flow is simulated with a mixture-model approach [29, 44]. Features like 6 degrees-of-freedom body motion simulation, cavitation and turbulent transition models, as well as multi-domain computations with sliding or overset meshes, are available but are not described here for brevity.

Mesh adaptation The adaptive grid refinement method included in ISIS-CFD [42, 43] performs isotropic and anisotropic h-refinement of unstructured hexahedral meshes, by dividing the cells of an original grid into finer cells. Original meshes used in ISIS-CFD are generated with HEXPRESSTM which is an unstructured full-hexahedral meshing tool developed by NUMECA Int. This leads naturally to adaptive refinement based on hexahedral division which is computationally cheap and can be called repeatedly during a flow computation. Also, the adapted meshes have good compatibility with ISIS-CFD without any need to modify the flow solver. The cell division can be repeated several times until the desired cell sizes are obtained, so the mesh is adapted regularly during the computation in order to follow the convergence of the flow; earlier refinements can be undone to account for the changes in the flow as it converges. The decision where to refine comes from a refinement criterion which is a metric tensor field $C(x, y, z)$ computed from the flow, following [11]. The mesh is refined until the dimensions $\mathbf{d}_{i,j}$ ($j = 1, 2, 3$) of each hexahedral cell i satisfy:

$$\|C_i \mathbf{d}_{i,j}\| = T_r, \quad (1)$$

where the constant T_r globally specifies the mesh size. The refinement criterion is based on the Hessian matrix of second spatial derivatives. Hessian matrices can be interpreted as error indicators, since they are linked to interpolation

errors for linear interpolation (see for example [22]). Thus, they provide a measure of the truncation error for a second-order finite-volume discretization. The Hessian $H(q)$, for a given state variable q , is a 3×3 symmetric tensor:

$$H(q) = \begin{bmatrix} q_{xx} & q_{xy} & q_{xz} \\ q_{xy} & q_{yy} & q_{yz} \\ q_{xz} & q_{yz} & q_{zz} \end{bmatrix}. \quad (2)$$

The Hessian matrix can be used directly as a tensor refinement criterion. In ISIS-CFD however, assuming that an indication of the local error is given by $H(q)$ times the cell sizes squared (which is reasonable for a second-order accurate discretization), equidistribution of this error indicator leads to [43]:

$$C = (\|H(q)\|)^n, \quad (3)$$

where $n = 1/2$. The absolute value of a matrix $\|\cdot\|$ corresponds to a matrix having the same eigenvectors as the original one and the absolute values of its eigenvalues. In the same way, the power n of a matrix is obtained by taking its eigenvalues to the power n while keeping the eigenvectors.

In order to adapt the mesh to pressure-based flows but also to boundary layers, wakes, and shear layers, the criterion is based on the Hessians of both the pressure and the velocity [42]. To give equal importance to the different Hessian matrices, a common weight ρU is assigned to all the velocity Hessians, where $U = \sqrt{u^2 + v^2 + w^2}$, and the criterion is chosen as:

$$C_{FCH} = (\max(\|H(p)\|, \rho U \|H(u)\|, \rho U \|H(v)\|, \rho U \|H(w)\|))^n. \quad (4)$$

The maximum of two tensors is computed using the approximative procedure from [43]. For free-surface flows, this criterion is combined with refinement at the water surface [41].

In ISIS-CFD, several measures are available to improve the regularity of the adaptively refined meshes. To prevent infinite refinement around flow singularities or close to large errors in the refinement criterion, a minimum cell size can be imposed, below which cells are never refined. Furthermore, refinement bounding boxes can be used to limit the regions where the automatic refinement is active and a boundary layer protection is available to preserve the column / layer structure of the boundary layer mesh.

On curved bodies, to prevent pressure perturbations and to ensure smooth solutions, the refined mesh is projected onto the correct geometry. After each adaptive refinement step, first the new boundary nodes are moved to the geometry, represented by a triangulation. Then the volumic mesh around these nodes is deformed locally: spheres are defined around each boundary node, in such a way that each sphere contains no other boundary nodes. The displacement of the boundary nodes is applied to all the nodes in each sphere, in a weighted manner such that the deformation goes to zero on the outside of the sphere. With this approach, the deformation for each boundary node is handled independently.

3. Adaptive grid refinement with averaged quantities

The issues of hybrid LES models on dynamically changing meshes (Section 1), all appear when turbulent flow features encounter temporal or spatial variations of the mesh size. Standard mesh adaptation leads to many such situations, which makes the use of adaptive grid refinement complicated with hybrid turbulence models. But on the contrary, adaptive refinement could be aimed at reducing the number of mesh size changes that the main flow features encounter, to limit the effect of the mesh on the performance of the turbulence model and to remove the interpolation errors as much as possible. This implies using AGR to produce stationary meshes that are uniform in the path of the main flow features.

The behavior of the adapted mesh is imposed by the refinement criterion, which determines which part of the mesh should be refined. Therefore, limiting the mesh evolution in time is possible by limiting the changes in the refinement criterion. In ISIS-CFD, the refinement criterion tensor (4) in the AGR process is usually defined from the instantaneous velocity and pressure fields at each refinement time step. Since the instantaneous solution evolves fast, particularly for highly unsteady flows, the criterion which is computed from this solution is influenced by its evolution, so the mesh changes to follow every eddy. The proposed option here is to compute the criterion based on an averaged solution instead of the instantaneous solution. Thus, the refined mesh only changes to follow the main unsteady flow features, while all the turbulent structures are captured on a mesh that remains nearly constant. For statistically steady flows, the grid adaptation converges to a static mesh.

Within this basic concept, several choices for the averaging strategy are possible. These are outlined below, and tested in the following Section 4 in order to identify the best approach. A more complete description of these choices is provided in [23, 24].

3.1. Averaged quantity

To limit the mesh changes during the adaptation process, AGR is performed based on an averaged refinement criterion. The question is how this averaged criterion should be obtained from the instantaneous flow solutions. Two different averaging approaches are investigated: in the first approach, the instantaneous flow fields (velocity and pressure fields) are averaged. Before each refinement step, the refinement criterion Eq. (4) is then computed based on these averaged fields. In the second approach, before each time step, the refinement criterion is computed from the instantaneous solution and averaging is performed over these instantaneous criteria. Then, in each refinement step, AGR refines or derefines the mesh based on the current average of the refinement criteria computed from the instantaneous solution.

Averaging the criterion is more expensive than averaging the flow fields, both in terms of computational cost and required memory. First, there is a performance penalty: the refinement criterion is computed before each time step, instead of only before the refinement. And second, the memory required is higher, since instead of 4 variables for the averaged solution (three for the velocities and one for the pressure), the 6 variables of the criterion tensor field must be saved.

3.2. Averaging interval

In addition to the effects of averaging approaches on the performance of the adaptation, the length of the averaging interval affects the intensity and the frequency of the fluctuations in the averaged criterion. Therefore, it determines the behavior of the AGR and thus the adapted mesh. Two different averaging methods are proposed based on the size of the averaging interval. In the first method, the averaging is applied over the entire computational time, and in the second one a sliding averaging window is selected which considers only the most recent part of the computational time. Different implementations are required for each of these averaging methods. In Fig. 2, the averaging schemes are presented. For averaging over the entire computational time, the instantaneous fields in each time step are summed and saved in a single set of tables (4 or 6 depending on the averaged quantity, see above). Before each refinement time step, the average value is computed by dividing the summation by the current number of time steps; this average is used to define the refinement criterion.

For a sliding window, in which the averaging is applied over a constant number of time steps, the averaging algorithm is more complex. In principle, the instantaneous solution of each time step needs to be saved separately to be used for the averaging. This is very expensive in terms of the required memory to save the solutions. But since the average solution is needed only at the refinement time steps, it is possible to reduce the number of tables by saving the average solution over intervals between refinement steps instead of saving the solution of each time step. In this case, the size of the sliding window must be a multiple of the interval between the refinements and a table will be required for each refinement interval in the sliding window. After each refinement step, the oldest table is overwritten with the criteria from the new interval. The length of the sliding window determines the number of tables required and also has a major influence on the behavior of the mesh adaptation, as seen in Section 4.4.

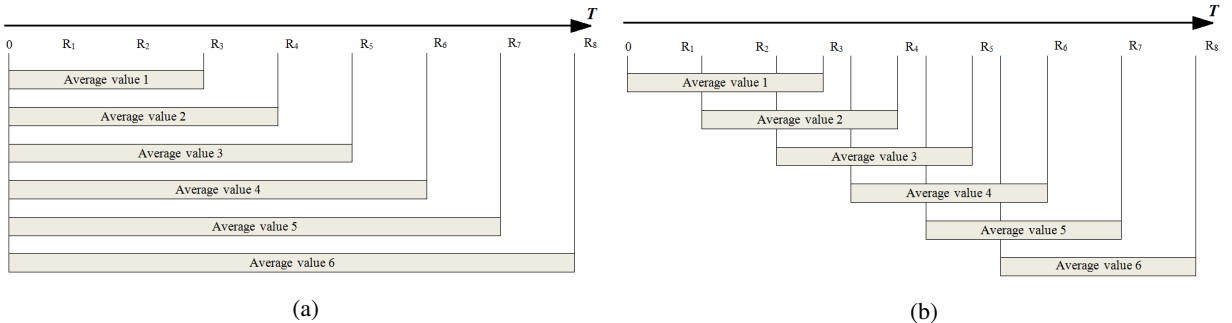


Figure 2: Averaging algorithms: The whole computation time (a), Sliding window with a specific number of time steps (b). R_i corresponds to a time step where the mesh is refined.

3.3. Choice of the refinement criterion

The choice was made here to use the same basic refinement criterion as for RANS simulation. In the ISIS-CFD solver, the pressure–velocity Hessian (FCH) criterion, as described in Eq. (4), gives an indication of the truncation error in the convective momentum equation fluxes. Based on the instantaneous flow field, it is used with confidence in RANS simulations. The use of this criterion for hybrid RANS/LES simulations, in the form of an averaged criterion, raises several questions.

The first question is, if it is acceptable to average this criterion. The use of an existing instantaneous criterion is a logical choice for the second approach in Section 3.1, where the averaging is performed over the criteria which are computed from instantaneous solutions. The idea of this approach is to satisfy the mesh sizes requested by the instantaneous criteria, in an average way. Thus, if the instantaneous criterion makes sense, the average criterion is effective too. No such theoretical motivation exists for the criterion based on the average solution. However, this approach is still interesting due to cheaper computation and less required memory.

The second question concerns the compatibility of the FCH Hessian criterion with hybrid RANS/LES simulations. To the best of authors' knowledge, no studies on evaluating or developing refinement criteria for this type of model, such as what has been done for LES [1, 4, 6, 34], have been conducted so far. A possible concern about the choice of a Hessian criterion is, that refining based on a truncation-error estimate may not be valid in a situation where the turbulence modeling depends on the mesh size. However, Toosi and Larsson [34] derive an almost identical criterion for LES starting from a directional equidistribution of the turbulence. Thus, in practice, the Hessian probably remains a valid choice. A second point concerns the absence of turbulent quantities in the definition of the criterion. Still, a criterion which works for RANS should function well in the RANS regions for hybrid models, while in the LES part, no modeled turbulence is present; the flow is dominated by velocity fluctuations, for which the criterion is designed.

A final question regarding FCH and similar criteria is, that they refine where the most intensive flow structures occur, while weaker eddies may be under-resolved. This may be invalid if there is a significant influence of the weaker structures on, for example, the destabilization of the larger structures. This issue will be investigated in the tests presented in the following sections.

4. Test of the criterion averaging settings

In the first test case of this study, the two averaging approaches of Section 3.1, the effects of changes in the refinement threshold (Eq. (1)) and the selection of the averaging interval (Section 3.2) on the final refined mesh and the solutions are studied. In addition, it is investigated how a change in the initial mesh affects the final solution. For this test, the average-based adaptation integrated in the ISIS-CFD solver is used with IDDES to simulate a turbulent backward-facing step flow which is a common and conventional test case in hybrid turbulence modeling.

4.1. Test case and reference computations

An IDDES simulation of a turbulent separated flow behind a backward-facing step is performed based on the experimental study by Vogel and Eaton [39]. This particular flow was widely used during the last decade to study the performance of hybrid turbulence models, particularly the IDDES model [14, 15, 32]. The objective of these studies was to model the attached boundary layer prior to the step and the boundary layer on the entire opposite wall in RANS mode, and after the flow separation, to have the model switch to LES mode.

The flow behind a BFS is complex and involves various unsteady features. The flow wake can be divided into three main regions (Figs. 3 and 12a): in the shear layer region, the separation from the tip of the step occurs and the shear layer is developed. In the reattachment zone, the shear layer structures touch the wall. Finally, in the relaxation region, an attached boundary flow is developed. The main turbulent structures are created by Kelvin-Helmholtz (K-H) instabilities in the shear layer. These small vortices amalgamate into larger vortices and create larger structures. This vortex pairing process continues and larger scale structures are created until they grow to the order of the step height and are being impinged on the wall at the reattachment point, in the reattachment region. This slows down their passing frequency and results in the gathering of the shear layer structures which increases their size. Then, these large coherent structures shed downstream in the relaxation region with no further amalgamation. This is referred to as the shedding mode. This short description will be helpful later in Section 4.4 where a frequency analysis over the BFS flow is performed.

The computational domain based on the step height H (see Fig. 4a), runs from $-4H$ to $20H$ in streamwise direction ($x = 0$ corresponds to the step location). In the spanwise direction, the size of the domain is $4H$ and the channel

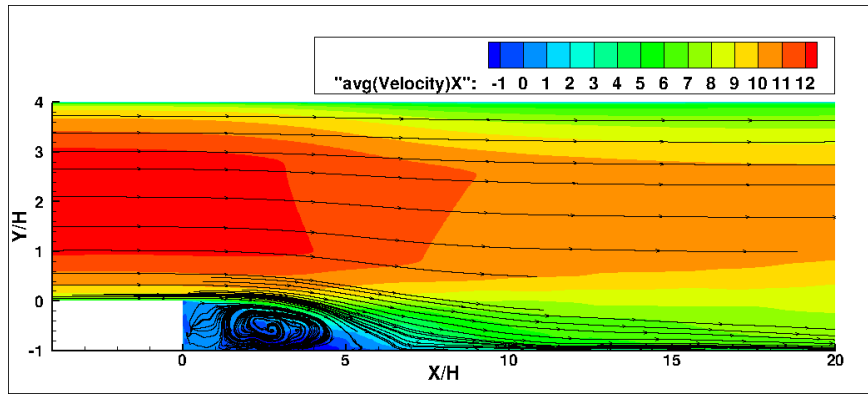


Figure 3: Averaged streamwise velocity and streamlines of reference IDDES simulation.

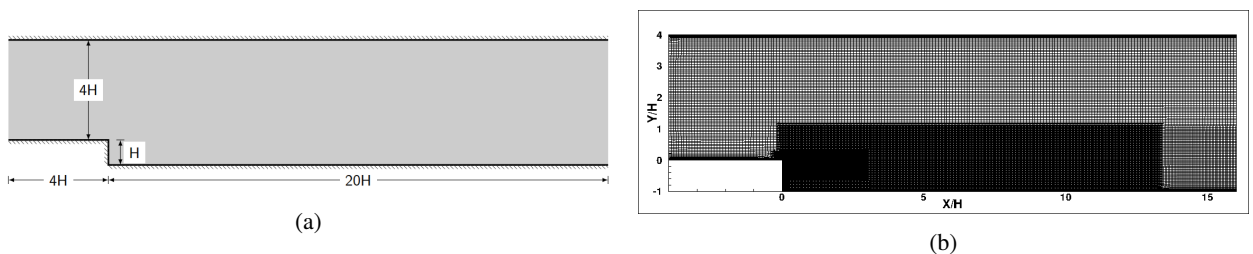


Figure 4: Backward-facing step; the computational domain (a), the reference fine mesh (b).

expansion ratio is $5/4$. At the inlet, the Reynolds number based on the step height, $H = 0.038 \text{ m}$, is equal to 28,000. Distributions of velocity and turbulence quantities at the inlet are specified from a precursor RANS calculation conducted for the channel flow and correspond to the experimental value of the boundary layer thickness at that location ($1.07H$). Mirror boundary conditions are specified in the spanwise direction. A no-slip condition is specified on the solid walls and on the outlet boundary a frozen pressure is applied. A non-dimensional time step of 0.018 is chosen to ensure that the CFL number over the entire domain remains less than one, especially at the vicinity of the step, where the streamwise cell spacing is minimum.

Computations using AGR begin with the entire computational domain covered with a coarse grid. The initial coarse mesh for the start of these simulations is presented in Fig. 5a. The maximum grid sizes in streamwise and spanwise directions are equal to $0.2H$ and to $0.1H$ respectively, which corresponds to $\Delta x^+ = 240$ and to $\Delta z^+ = 120$ in wall units. The mesh is uniform in the spanwise direction (the number of cells is 40). For reference computations, a static fine mesh was also generated (Fig. 4b) similar to the mesh used by Shur et al. [32]. It has appropriate clustering near the walls and in the vicinity of the step. Several refinement boxes are used to reduce the mesh size behind the step around the free shear layer area. The maximum grid sizes in streamwise and spanwise directions are half of the initial coarse mesh of the computations using AGR, which corresponds to $\Delta x^+ = 120$ and to $\Delta z^+ = 60$ in wall units. This mesh has 80 uniform cells in the spanwise direction. Finally, the reference mesh contains 9.2×10^6 cells in total compared to around 5×10^5 cells in the initial coarse mesh.

Reference simulations In the following, several computations are performed to test the variation of the averaging strategy and of the interval. The results are compared with the experimental data and also with two computations: one that uses the fixed fine mesh without AGR, and one using AGR without averaging (*AGR-100*). In the computation *AGR-100*, the refinement is applied every two time steps, unlike the computations with average-based AGR, in which the number of the time steps between two consecutive refinements is set to 25.

The highly unsteady flow causes the refinement criterion for the computation *AGR-100* to change constantly. Thus, the mesh (Fig. 5b) is modified often. Fig. 6a shows the evolution of the number of cells due to the refinement. The number of cells increases to around 20 million at certain moment, which is much higher than the number of cells for

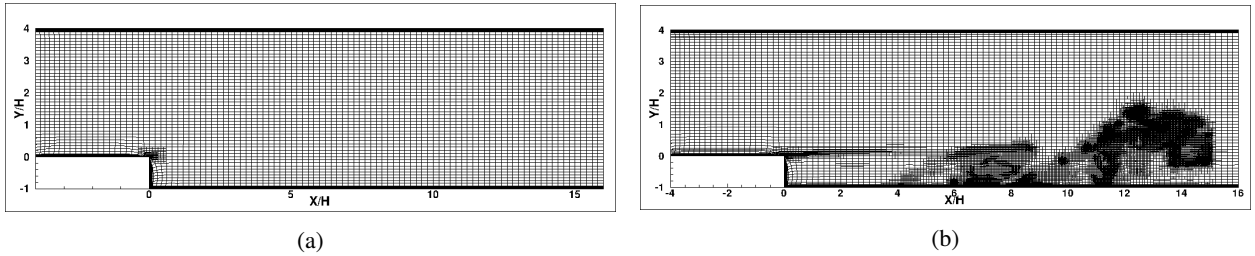


Figure 5: Backward-facing step: initial coarse mesh (a), AGR based on instantaneous solutions *AGR-100* (b).

the computation with a fixed reference mesh (Table 2). In Fig. 8, perturbations are seen in the mean skin friction coefficient ($C_f = \frac{\tau_w}{1/2\rho U_\infty^2}$) along the lower wall for *AGR-100*, compared to the experimental result and the reference simulation with the fine fixed mesh, even though the AGR follows the turbulent structures and refines the mesh in the regions where unsteadiness is high. This confirms the need for a time-averaging process to limit the changes of the criterion and to better control the mesh evolution.

Table 1

Properties of the performed simulations, CA: Criterion of Averaged flow field, AC: Average of the instantaneous criterion.

Computation name	Averaging method	Interval (time step)	T_r
Fine (fixed mesh)	-	-	-
AGR-100	No Averaging	-	0.01
CA@-25	Time-averaged Flow field	all	0.0025
AC@-25	Time-averaged Criterion	all	0.0025
AC@-20	Time-averaged Criterion	all	0.0020
AC@-15	Time-averaged Criterion	all	0.0015
AC50-25	Time-averaged Criterion	1250	0.0025
AC01-25	Time-averaged Criterion	25	0.0025
AC@-25B1†	Time-averaged Criterion	all	0.0025
AC@-25B2†	Time-averaged Criterion	all	0.0025

† A refinement box is added to the initial mesh.

All the computations and their conditions are given in Table 1. For the computation label, the two beginning capital letters correspond to the averaging approach which is used in the simulation: «CA» indicates the Criterion based on the Averaged flow fields and «AC» for the Average of the instantaneous Criterion. The size of the sliding averaging window is specified by the number of tables used for saving the values, or by «@» which indicates the entire computational time. The last two digits on the right side of the code are related to the refinement threshold.

4.2. Average of the flow fields / average of the criterion

In this first test, the two approaches for computing an average-based refinement criterion are compared. Both averaging approaches start from the same coarse mesh and use the same simulation conditions. The simulations are indicated in Table 1 by the codes CA@-25 and AC@-25. The computations run for 2500 time steps to remove the transient effect of the flow, without any refinement. Then the averaging process starts and once the averaged solutions have been computed over the first 25 time steps, the refinement is applied for the first time. For this simulation, the refinement is applied every 25 time steps and the averaging interval is the entire computational time (7500 time steps max), so only one set of tables is enough to save the averaged values. With respect to the computation *AGR-100* with $T_r = 0.01$, since averaged quantities are used for the refinement, the magnitude of the criterion components is reduced. Thus, with the same threshold (0.01), according to Eq. (1) the requested cell sizes would increase. To keep a similar number of cells, the threshold is therefore lowered to $T_r = 0.0025$.

The number of cells increases after the AGR is applied for the first time (at time $T = 0.15$) in both computations CA@-25 and AC@-25 (Fig. 6a). This increase is far less than for the computation *AGR-100*, even though the threshold

Average-based mesh adaptation

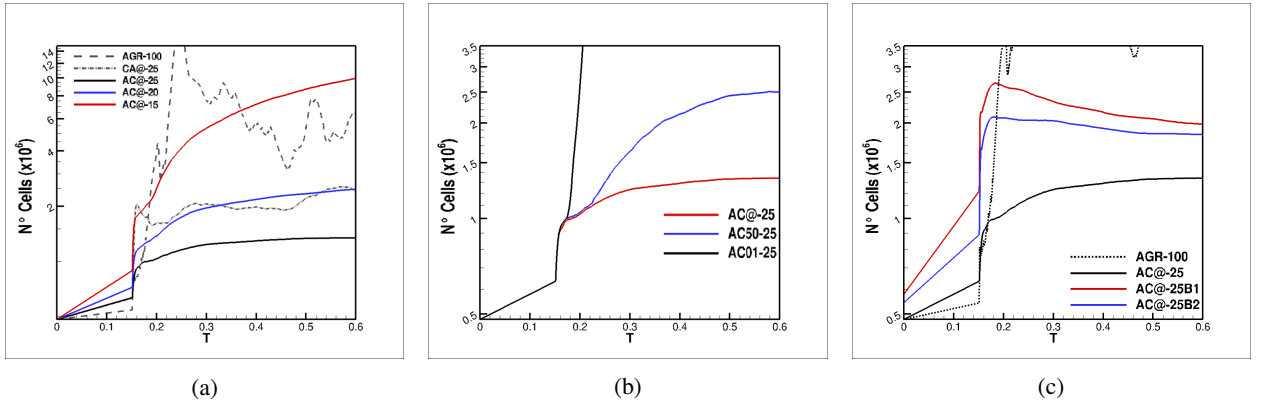


Figure 6: The changes in the number of cells due to the adaptation process during the computational time for the computations with different: thresholds (a), averaging intervals (b) and initial meshes (c).

is lower for these two simulations. In addition, the variation in the number of cells during the computations is not the same. For the computation *AC@-25*, the rate of increase is gradually reduced until the mesh converges to a constant number of cells (1.3 million cells in Table 2), almost half the number of the cells in the computation *CA@-25* where the mesh never becomes steady. The final refined mesh in Fig. 7 for both simulations shows that the refinement is performed around the shear layer, in the reattachment region, in part of the relaxation region and in the vicinity of the walls. The mesh in the region between the shear layer and the lower wall, the so called recirculation zone, remains coarse due to the low flow rate.

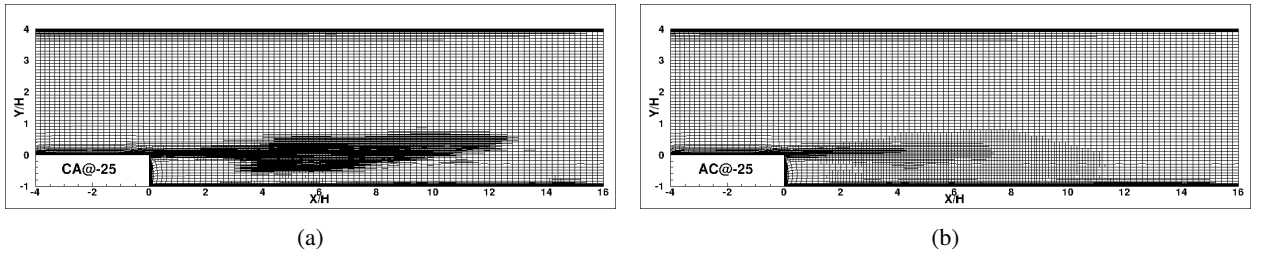


Figure 7: The adapted refined meshes for the two averaging strategies: *CA@-25* with time-averaged flow field (a), *AC@-25* with time-averaged criterion (b).

The mean skin friction coefficient distribution along the walls for these two simulations is presented in Fig. 8. This figure shows that the solution is improved with respect to *AGR-100*, especially in the reattachment and the relaxation regions where most of the refinement is performed. This improvement is more prominent for the computation *CA@-25* since the adapted mesh is finer compared to the computation *AC@-25*. The reattachment length is predicted around $X/H = 7.14$ and the difference with experimental data is reduced from 25% for *AGR-100*, to little more than 7% (Table 2).

Despite the somewhat acceptable results of adaptive refinement based on the averaged flow field (*CA*), the mesh in the refinement regions is not regular (Fig. 9). These irregularities come from the interpolation process for transferring the averaged solution from the coarse grid to the finer grid, during the mesh refinement. Since the interpolation is linear (C_1), the derivative of the interpolated solution is discontinuous on the boundaries of the coarse cells and thus the second-derivative based refinement criterion is high, which means that those regions are refined excessively. In addition, the adaptation based on the averaged flow is not adequate for simulating the instantaneous flows at all times. For instance, the average flow may have a thin shear layer, whereas the instantaneous flows could have much thicker vortex structures. Thus, a thicker refinement zone is needed to capture these structures, which is unlike what is achieved through refinement based on averaged solutions.

By comparing both approaches, it can be concluded that the refinement based on the average value of the instantaneous criterion is the most suitable choice. This approach removes the irregularities in the mesh and reduces the

Average-based mesh adaptation

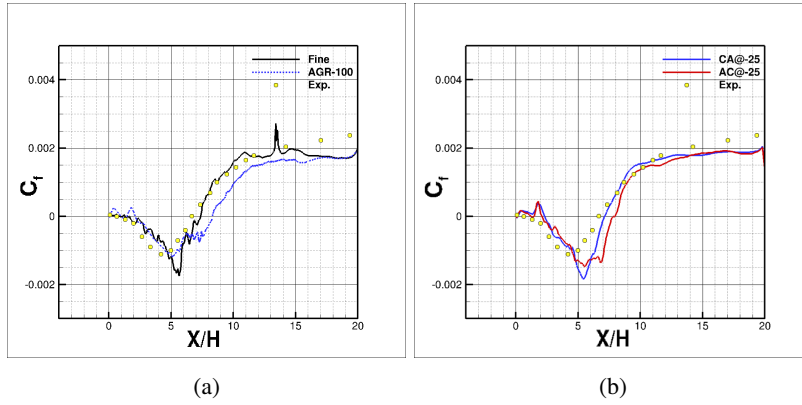


Figure 8: Mean skin friction coefficient distributions along the lower wall: *Fine* and *AGR-100* (a), *CA@-25* and *AC@-25* (b).

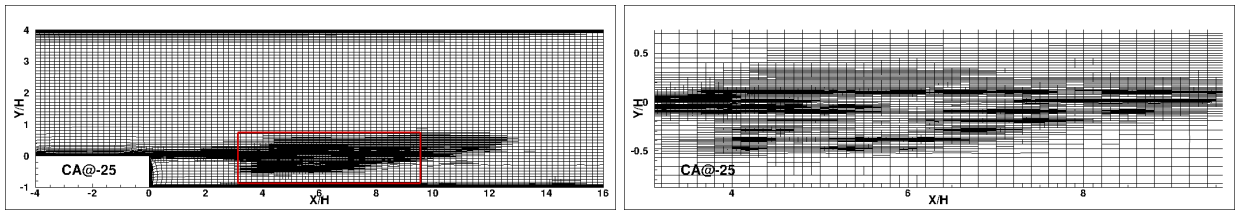


Figure 9: The irregularities of the final adapted mesh for refinement based on the averaged flow field (*CA@-25*).

Table 2

Number of cells and reattachment length at the end of the simulations.

Computation	N° Cells ($\times 10^6$)	L_r (X/H)	Error (%)
Exp.	-	6.66	-
Fine	9.3	7.3	9.6
AGR-100	6.6	8.35	25
CA@-25	2.4	7.14	7.2
AC@-25	1.3	7.9	18.7
AC@-20	2.5	7.0	5.1
AC@-15	9.9	6.9	3.6
AC50-25	2.5	7.7	15.6
AC@-25B1	2.0	6.5	-2.5
AC@-25B2	1.8	6.3	-5.4

variation in the number of cells. Furthermore, since the adapted mesh must resolve the instantaneous flow at all instants, it makes sense that the mesh refinement is based on instantaneous refinement criteria (in an averaged sense). Although the solution of the computation *AC@-25* is still far from the reference simulation and the experimental data, it can be improved by lowering the threshold to obtain more refinement in the whole domain.

4.3. Threshold effect

As seen above, the final refined mesh for AGR based on the average of the criterion is too coarse to capture the flow details. To increase the resolution of the mesh globally, the user-specified refinement threshold can be lowered. Two new computations *AC@-20* and *AC@-15* are performed with the same computational conditions as *AC@-25* but with lower thresholds values $T_r = 0.002$ and 0.0015 (Table 1). As a result, the mesh becomes finer particularly in the shear layer and the reattachment regions (Figure 10). In the relaxation region, the mesh density increases until $X/H = 15$, where further refinement is forbidden by a limiting box. Finally, the grids are finer in the vicinity of the walls and for

$T_r = 0.0015$, the outer edges of the boundary layers are fully captured by AGR. Due to this increase in the refinement, the mesh contains almost 2.5 million cells for simulation $AC@-20$ and 10 million cells for $AC@-15$ at the end of the computation.

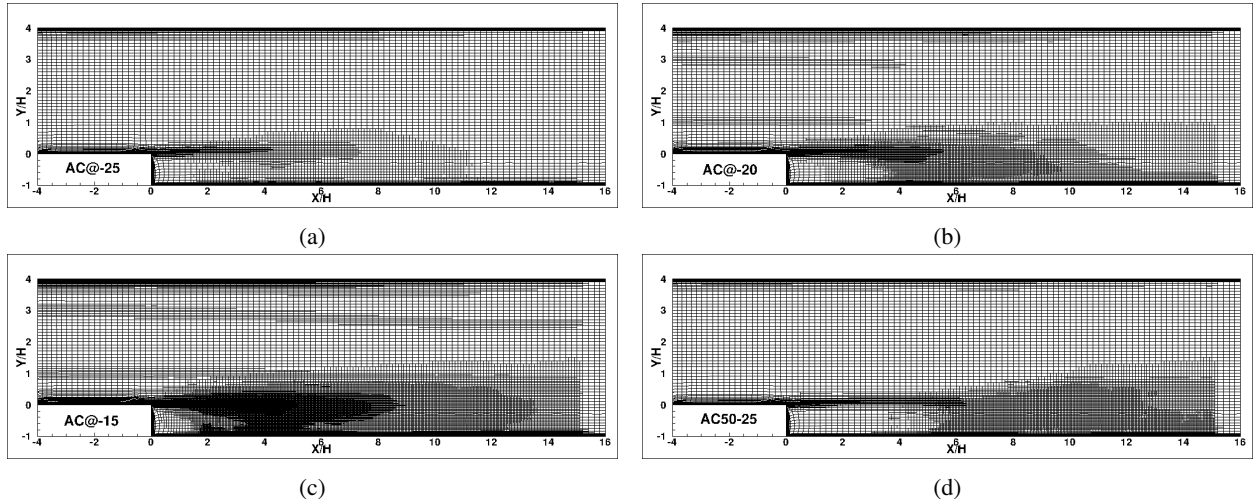


Figure 10: The adapted refined meshes for the computations with the time-averaged criterion: $AC@-25$ (a), $AC@-20$ (b), $AC@-15$ (c) and $AC50-25$ (d).

On one hand, a high-resolution mesh is undesirable in terms of computational cost. On the other hand, such a mesh increases the accuracy of the solutions compared to simulations with higher thresholds. The error in the reattachment length for $AC@-20$ is a bit more than 5% with only 2.5 million cells, while the significant increase in the mesh size for simulation $AC@-15$ leads to 3.6% error of the reattachment length (Table 2).

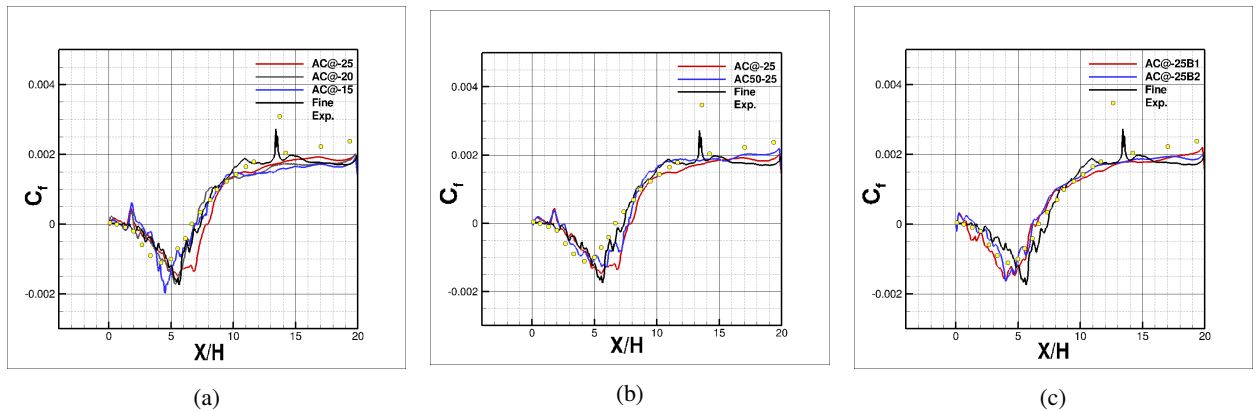


Figure 11: Mean skin friction coefficient distributions along the lower wall for the computations with different: thresholds (a), averaging intervals (b) and initial meshes (c).

The distribution of the mean skin friction coefficient is also affected by the increase in the mesh resolution. As the threshold is lowered, the solutions get closer to the experimental data especially in the reattachment and the relaxation regions (Fig. 11a). For these computations, the iso-surface non-dimensional second invariant for $Q^* = 2500$ is presented in Fig. 12. It shows how the reduction of the threshold leads to more creation of turbulence in the entire computational domain. For simulation $AC@-15$, the vortices in the shear layer are better represented and a rolling up of the vortex sheets is observed. The small-size structures in the recirculation zone close to the reattachment point are also captured (Fig. 12d). However, even by lowering the threshold, AGR is not able to capture small eddies in the forward recirculation zone and the local mesh remains coarse. This may be the reason for the overestimated skin friction in this zone (around $X/H = 2$).

Average-based mesh adaptation

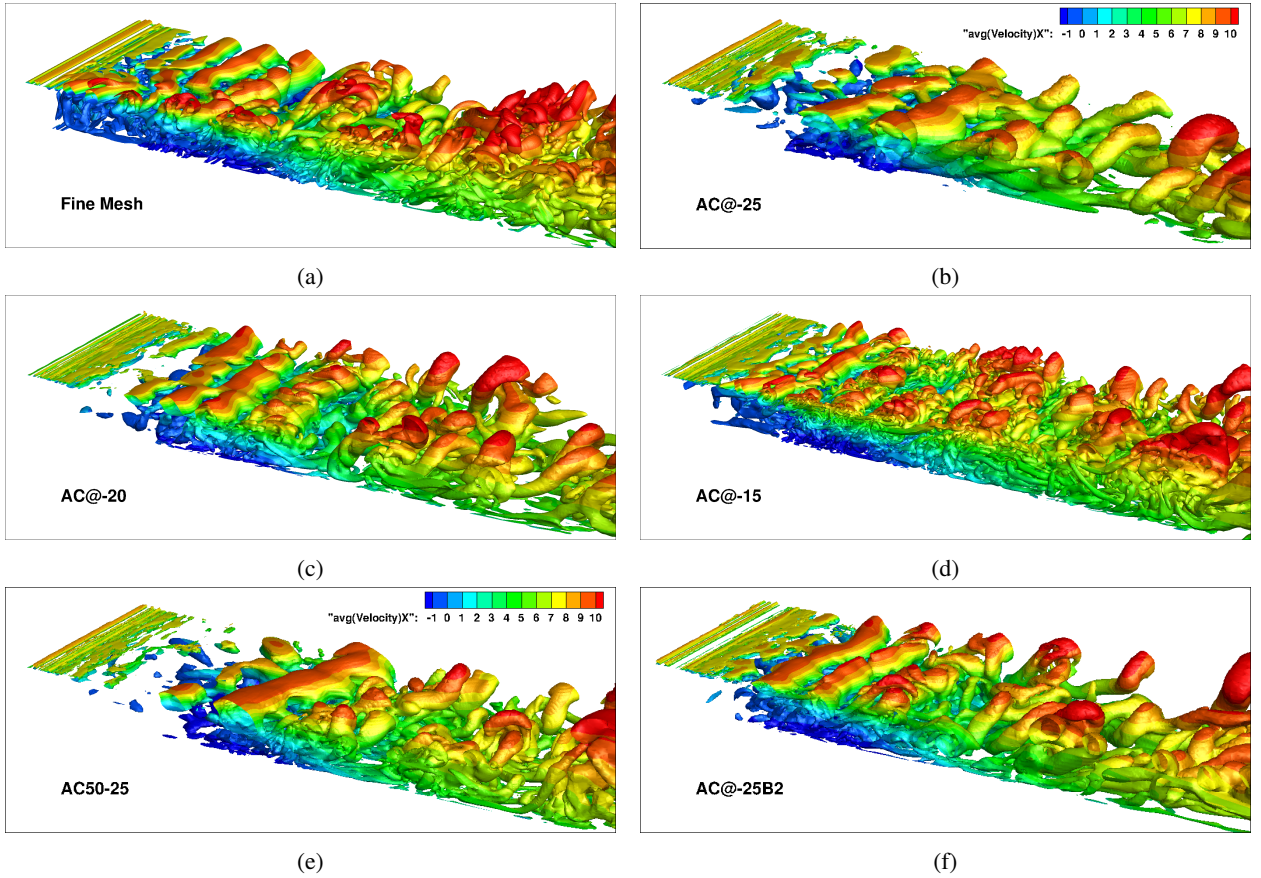


Figure 12: Iso-surface of the non-dimensional second invariant $Q^* = 2500$ colored by averaged X -velocity: *Fine* (a), *AC@-25* (b), *AC@-20* (c), *AC@-15* (d), *AC50-25* (e) and *AC@-25B2* (f).

To sum up: the reduction of the threshold confirms the validity of the averaged-criterion mesh refinement procedure, since the solution converges towards the *Fine* result and the experiments when the adapted mesh is refined. Of course, the improvements in the solution as a result are accompanied by an increase in the computational effort. Therefore, to have an optimal threshold for these simulations that gives a reasonable approximation of the reference solution, a compromise between the accuracy of the solution and the computational effort must be searched.

4.4. Averaging interval effect

So far, all the final refined meshes are based on refinement criteria averaged over the entire computational time (7500 time steps). Time-averaging over the whole computational time is the easiest but not always the best choice. It implies a large influence of the initial transient flow features on the averaged solution and a low rate of change of the averaged criterion, which causes the mesh adaptation to occur slowly. Instead, the averaging can be applied over a shorter sliding window. Reducing the size of the averaging interval increases the rate of change in the averaged solution, since a smaller interval removes transient effects faster. This allows the AGR to be more reactive and adapt the mesh quicker, leading to faster convergence. Also, there may be slow unsteady features in the flow, which could be captured by a dynamically changing adapted mesh using less cells than a stationary mesh suitable for all instants. This can be obtained by a sliding window average as well.

The selection of an effective interval size gives interval averaging an advantage over using the entire computational time. To have an idea about the right size of the averaging interval, the physics of the flow should be considered. It is important to know what unsteady features exist in a flow and which one is dominating. Then, based on their frequencies, it can be decided which ones will be averaged out and which ones will be followed by the adaptive meshing.

BFS flow frequency analysis As described in Section 4.1, the flow behind a BFS involves various unsteady features and instabilities. These instabilities occur over a wide range of frequencies. A time signal analysis is performed for the instantaneous velocity at several positions of the domain in the fine-grid reference simulation (called *Fine* in Table 1, see Section 4.1), to determine the frequencies of the locally dominating flow features (Fig. 13). These flow features and motions are described using the Strouhal number, given by $St_h = fH/U_\infty$, where f is the mode frequency, H is the step height and U_∞ is the free stream velocity.

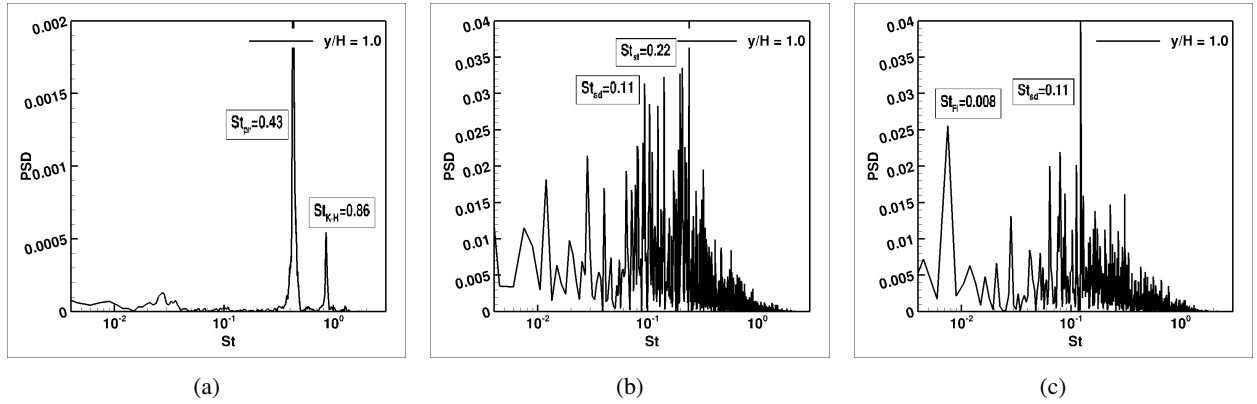


Figure 13: Power spectral density of the velocity in Y -direction at: $X/H = 0.52$ (a), $X/H = 6.67$ (b), $X/H = 15.8$ (c).

In the shear layer region (Fig. 13a), the two peaks correspond to the high-frequency structures of the initial small scale vortices which are created due to the Kelvin-Helmholtz instability ($St_{K-H} = 0.86$) and the merging process of these small vortices through vortex pairing ($St_{pr} = 0.43$). These frequencies are consistent with the observations of Hu et al. [18] on a similar BFS test case. Going downstream, the domination of the vortex pairing reduces and new features stand out. In the reattachment region (Fig. 13b), $St_{st} = 0.22$ is related to the step mode which is the lowest frequency of the vortex pairing where the amalgamated vortices have reached the size of the step. The shedding mode $St_{sd} = 0.11$ is related to even more amalgamated structures which separate from the bottom wall. For the position in the relaxation zone (Fig. 13c), the dominating frequencies are related only to shedding. In addition, another low frequency feature is detected which corresponds to a roughly two-dimensional flapping motion of the initial part of the shear layer in the vertical direction [17] that causes the oscillation of the reattachment point of the shear layer on the lower wall. Among all the unsteady flow features in BFS flow, the lowest frequency corresponds to this flapping motion ($St_{fl} = 0.008$). The periods of these low-frequency flow features correspond to about 500 time steps for the shedding mode and 7000 time steps for the flapping motion.

To see how these high-to-low frequency flow features affect the time evolution of a sliding-window averaged solution, the changes in the averaged velocity of these locations with different averaging intervals are presented in Fig. 14. For the averaging interval of 1000 time steps, which is twice the period of the shedding mode, the large fluctuations due to higher frequency flow features than the shedding, such as the Kelvin-Helmholtz instability and the vortex pairing, have completely disappeared (Fig. 14a). Further increasing the averaging interval reduces the effects of the lower frequency fluctuations and limits the amplitude of the changes in the averaged velocity. It is implied that these increases will ultimately lead to the complete elimination of fluctuations from the mean solutions. This behavior is seen for all the positions.

In general, knowing the physics of the flow facilitates the selection of the averaging interval. The frequencies of the flow features can be used as options for the size of the averaging interval, or at least give a better understanding of the adaptation behavior. For instance, if a large averaging length of 10-15 periods or 5000-8000 time steps is used for this BFS case, the effect of a chaotic behavior like the shedding will appear in a purely averaged manner in the refinement criterion, while the effect of the very low-frequency flow features like the flapping motion will still be visible in the temporal evolution of the criterion. In the following, several averaging intervals are selected based on the discussed frequencies for the BFS flow. Then, the behavior of the adaptation process and the final solution of each computation are studied.

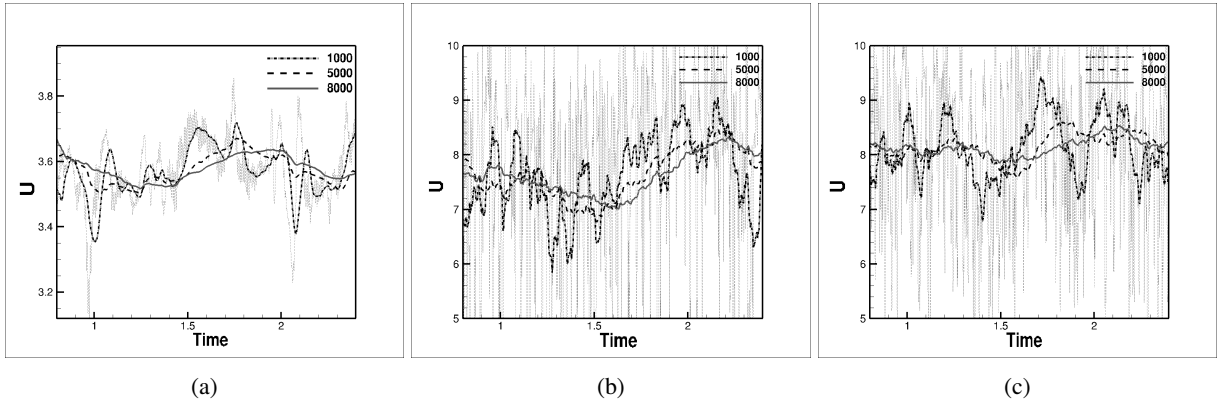


Figure 14: Sliding-window averages of the streamwise velocity evolution at: $X/H = 0.52$ (a), $X/H = 6.67$ (b), $X/H = 15.8$ (c) and $Y/H = 1.0$. The gray dotted line is the unfiltered signal.

AGR based on sliding windows To study the effect of sliding-window averaging, two simulations *AC50-25* and *AC01-25* are performed. In both simulations, the refinement is applied based on the average of the criterion and the threshold is $T_r = 0.0025$. The difference is only in the length of the sliding interval. For the simulation *AC01-25*, the averaging is applied over an interval which is equivalent to the distance between two consecutive refinements (25 time steps). This short interval is less than one period of the K-H instability in the shear layer. For the other computation *AC50-25*, the averaging interval contains 50 refinements, therefore the size of the interval is 1250 time steps, which corresponds to 2.5 periods of the shedding mode.

The first effect of the reduced interval is an increase in the number of cells in the final refined mesh (Fig. 6b, Table 2). In simulation *AC50-25*, the mesh at the end of the computation contains twice the number of cells of the equivalent simulation *AC@-25* with averaging over the entire computational time. This increase in the number of cells has two reasons. On one hand, the refinement criterion (and thus the mesh) converges faster to the average of the statistically steady flow, which leads to more refinement in the relaxation region and less refinement in the recirculation zone (Fig. 10d). Thus, it is expected that the case *AC@-25* will converge to the same adapted mesh if the computation is continued. On the other hand, since the averaging interval is reduced to 1250 time steps, the flow field fluctuations have a stronger effect on the average of the refinement criterion and strong vortices whose effect is not smoothed out by the averaging, may locally increase the refinement criterion. These effects are greater for the flow features whose frequencies are close to the size of the sliding interval, such as the shedding mode. Thus, more refinement is applied in the regions where these unsteady features are most pronounced. As a result, for the other case (*AC01-25*), the increase in the number of cells was such that the computation became too expensive to continue and was stopped manually.

For *AC50-25*, the distribution of the mean skin friction coefficient in Fig. 11b shows improvement in the reattachment and relaxation regions. In addition, the error of the prediction of the reattachment length (Table 2) is slightly smaller than for *AC@-25*. The iso-surface Q criterion of this simulation (Fig. 12e) is very similar to *AC@-25* (Fig. 12b), except for the relaxation region in which more smaller-size turbulent structures are created due to the local refinement in this region. Therefore, it seems likely that *AC@-25* is not fully converged and that the sliding window has accelerated the mesh convergence.

Thus, for sliding-window averaging, due to increased effects of individual flow features on the averaged criterion, more refinement and more mesh changes appear in the refined regions. This may or may not be a desired effect. Furthermore, a shorter interval causes the mesh adaptation to react faster to the flow evolution, so the convergence of the mesh is obtained faster than for the simulations with the averaging interval equal to the entire computational time. It is also shown that knowledge of the typical frequencies for the main flow features is useful for selecting the interval length.

4.5. Influence of the initial mesh

In all the previous simulations with AGR, no matter which averaging approach is performed or what the size of the averaging interval is, the refined grids are locally coarse in the recirculation zone (Figures 7 and 10). The reason for this is the inability of the refinement criterion to detect the small turbulent eddies in the recirculation zone. Since the

rate of flow in this zone compared to other parts of the domain is very low, the local value of the refinement criterion which is the second derivative of the flow field, is not large enough to lead to any refinement in the recirculation zone.

The question here is, what influence this coarse mesh in the recirculation zone has on the overall solution for the BFS flow. Two possible answers can be assumed for this question. First, the small eddies in the recirculation zone may have an effect on the shear layer. If these small eddies recirculate into the shear layer and cause it to be destabilized sooner, the location of the reattachment point will be incorrect on a coarse mesh for which these eddies are missing. If this hypothesis is confirmed, the converged solution would be perturbed by the coarse mesh. The second answer could be the slow generation of LES content in time. Until the mesh is refined around the shear layer and becomes fine enough to switch the turbulence model from RANS to LES, the separation is modeled by RANS and there is no resolved turbulence available in the region. Thus, with an initial coarse mesh, the solution of the downstream regions could develop slowly, although it eventually converges to the correct solution.

To understand the importance of each assumption and to see which one has a greater impact on the downstream solutions, two simulations *AC@-25B1* and *AC@-25B2* are performed which are based on *AC@-25*. The only change is, that two different refinement boxes have been added to the initial coarse meshes. For *AC@-25B1*, a refinement box is added in a part of the recirculation zone and the shear layer, while for *AC@-25B2*, the refinement box covers only the shear layer (Fig. 15). Thus, the first refinement box captures the small-scale turbulence in the recirculation region and resolves the shear layer, so it could trigger both effects. For the second refinement box, since the recirculation region flow moves in circles, any small-scale turbulence is removed by the coarse grid below the step. Thus, in the second simulation, only the effect of the faster generation of the LES content is investigated.

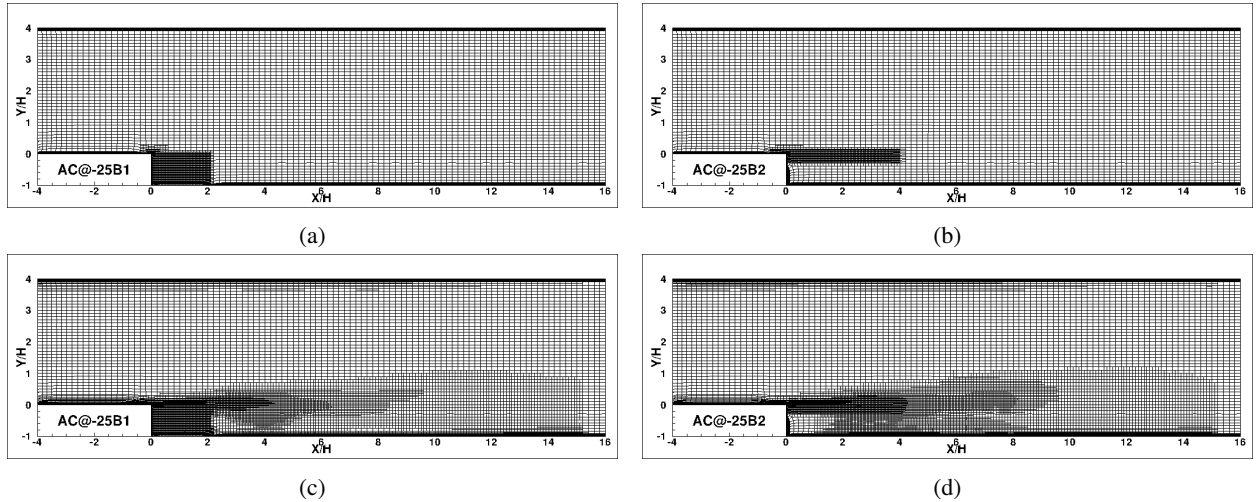


Figure 15: The effect of the refinement box in the recirculation zone. for *AC@25B1*: initial mesh (a), final adapted mesh (c); for *AC@25B2*: initial mesh (b), final adapted mesh (d).

By using the refinement boxes, a finer mesh compared to the computation without refinement box is obtained (Fig. 15, compare with Fig. 7b) and the refinement extends further downstream. The final converged meshes for both simulations have around 2 million cells (Fig. 6c). The quick increase in the number of cells in both simulations is indicative of a faster transient due to the initial mesh refinement in the shear layer. The distribution of the mean skin friction coefficient in the reattachment and relaxation zones is improved for both simulations with respect to *AC@-25*, as a result of the better representation of the shear layer by adding the refinement boxes (Fig. 11). The new results are in good agreement with both the reference fine-mesh simulation and the experimental results.

The similarity of the two final meshes in Fig. 15 confirms that it is the removal of the transient effect, rather than the small-scale eddies in the recirculation zone, which leads to the high-resolution refined meshes in the relaxation region, compared to the final mesh of *AC@-25*. The computations start with a fine grid behind the separation point and around the shear layer. The resolution of the mesh in these regions is high enough to activate the LES behavior of the turbulence model even during the first 2500 time steps which are dedicated to removing the transient flow. This is not the case for *AC@-25* which starts with an initial coarse mesh without any refinement box. The better representation of the shear layer for *AC@-25B2* in Fig. 12f compared to the solution of *AC@-25* confirms the effectiveness of the

presence of the refinement box in the shear layer region. This box gives the flow the possibility to immediately develop resolved content to represent the shear layer. The propagation of this turbulent content toward the downstream region causes more refinement in the reattachment and the relaxation regions.

Thus, although the small eddies in the recirculation zone play some role in the improvement of the solution (particularly the mean skin friction coefficient), for the entire flow field, the rapid resolution of the shear layer which is made possible by a refinement box around the separation point and the shear layer, is the most effective parameter in improving the results. This has two important implications. First, it validates the concept of refining where the most intense flow features occur, which is the underlying principle of a refinement criterion like Eq. (4). This is an indication that the use of refinement criteria developed for RANS, combined with averaging, makes sense for hybrid RANS/LES models (Section 3.3). And second, it shows that an initial fine mesh around the main flow features can improve the mesh convergence speed. To avoid the manual addition of refinement boxes, an option is to start the hybrid RANS/LES simulations from a converged RANS solution with adaptive meshing.

5. Complex-flow tests

In the next part of this study, hybrid RANS-LES and average-based adaptive refinement are applied together for the simulation of two realistic complex flow test cases. While the BFS test was aimed at finding the best settings and procedures for the average-based refinement, the main objective for the next cases is to test the ability and reliability of the average-based adaptive refinement in capturing the evolving flow structure for such complex flows.

5.1. Trailing vortices behind a ship

The first test concerns the DTMB 5512 ship model in steady sideslip conditions (combined sideways and forward motion), studied in the collaborative project NATO/AVT-253. Due to the sideslip, strong longitudinal vortices are created on the sonar dome in front of the ship and the bilge keels on its sides (Fig. 16). Experiments at Iowa Institute of Hydraulic Research (IIHR) [45] found a high level of turbulence kinetic energy (TKE) in the cores of these vortices. RANS simulations underestimate this TKE by a factor of 10 to 100. Using DES simulations, Visonneau et al. [36, 37] show that the vortex cores consist of highly dynamic, unsteady horseshoe-like vortices that rotate around the vortex center and are responsible for most of the TKE observed in the experiments. Traditional turbulence models like RANS cannot predict this behavior.

Since the vortex positions were not known in advance, the mesh creation for [36] was challenging. The final 163M cell mesh has two manually-placed refinement zones for the sonar dome vortex, with the finest extending from the sonar dome up to 0.6 times the ship length L . This zone has a mesh size of 0.6mm or $\lambda_T/4$, where λ_T is the Taylor micro-scale, an intermediate scale which can be defined as the upper bound of an inertial cascade. This mesh was created after several earlier computations determined the vortex position and showed that coarser meshes were insufficient to capture the vortex core dynamics.

The purpose of the current test is to duplicate the results provided by Visonneau et al. [36] in a single simulation, for which only the geometry is captured with fine cells on the original mesh, while all fine cells needed to follow the vortical wake are added by adaptive refinement. This section studies the adaptation strategy, the quality of the solution, and the convergence speed of the mesh adaptation.

Test case and settings The DTMB 5512 ($L = 3.048\text{m}$) is simulated at $V = 1.53\text{m/s}$, $Fn = 0.28$ and $Re = 4.65 \cdot 10^6$ with 10° sideslip to port. Like for the simulations in [36], the computation is started with RANS using the anisotropic EARSM turbulence model [8] and a time step of $\Delta t = 2 \cdot 10^{-2}\text{s}$. This precursor computation provides a mesh with initial refinement, which accelerates the convergence (Section 4.5). After 26 non-dimensional time units (t^*/L), the turbulence model is switched to a SST version of DDES [33] with a reduced $\Delta t = 5 \cdot 10^{-4}\text{s}$. The fluxes are discretized with a blended upwind – central scheme that uses 20% upwind. A no-slip (wall-resolved) boundary condition is applied on the hull, while the initial grid for the mesh adaptation has 15M cells and $y^+ = 0.13$ for the first layer of cells.

For the average-based mesh adaptation, the threshold is $T_r = L/20$ which is known to give fine meshes for RANS. To have a uniform mesh similar to the fixed fine mesh in the vortex cores, a minimum cell size for the refinement is set at 0.6mm; cells that have this size are no longer refined. Averaging of the criterion (AC) is used; the refinement criterion is based on the average of instantaneous criteria computed every 5 time steps. To obtain rapid convergence of the mesh, the DDES-SST simulation is started with sliding window averaging (Section 4.4). Since the original computations [36] show that the average period of the large turbulent eddies is about 80 time steps, a sliding window

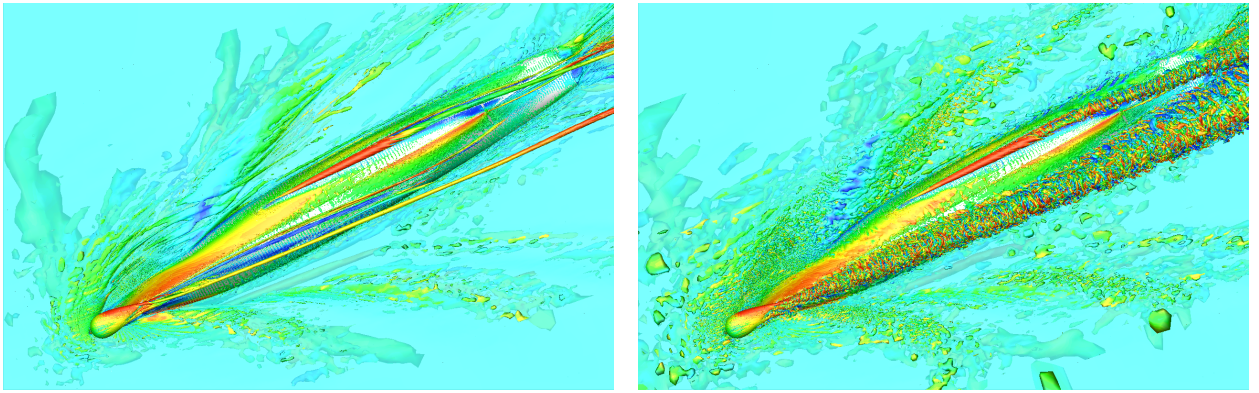


Figure 16: DTMB 5512. Iso-surfaces of the time-averaged (left) and instantaneous (right) (non-dimensional) $Q^* = 50$, seen from below, for DDES-SST simulation.

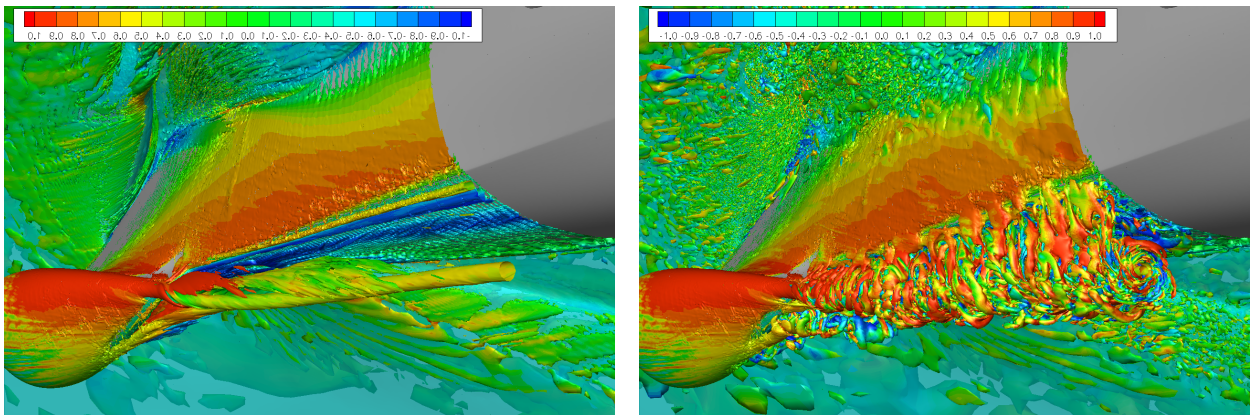


Figure 17: Cross-section at $x/L = 0.3$ of the time-averaged (left) and instantaneous (right) (non-dimensional) $Q^* = 50$ isosurface.

of 250 time steps was chosen to filter them out. However, as the preceding analysis shows, this averaging period of about 4 periods still creates time-dependent perturbations in the criterion. Therefore, to obtain a stable, smooth final mesh, a switch to averaging over the whole computation is made after 1.0 time units. The simulation runs for 2.5 time units with DDES-SST. The mesh refinement is performed every 50 time steps.

The original computations were run on 1300 processors and the adaptive ones on 840 processors. The approximate CPU times per computation for the original EASM (163M cells) and the adaptive EASM computation with the converged mesh of 47M cells are, respectively, 30 000 h and 16 000 h. Regarding the hybrid simulations, the CPU time is 160 000 h for the DDES adaptive (154M cells) computation, compared to approximately 250 000 h for the original DDES (163M cells) computation (these numbers do not include the RANS precursor computations.). The CPU time for the original DDES computation includes many extra time steps for additional analysis, which were not done for the adaptive refinement. So the adaptation probably saves some time, but not a lot.

Turbulent flow solution The average and instantaneous second invariant of the velocity Q^* (Fig. 16) show the main vortices coming from the sonar dome, the windward bilge keel, as well as the wake of the aftship. A detail of the sonar dome vortex (Fig. 17) indicates that the main vortex structure is formed by ring-like vortices which are shed from the destabilization of the shear layer starting from the vertical plane of symmetry and from separation bubbles on the leeward sonar dome side (not visible in this view). All these structures rotate around the center of the main vortex, creating significant fluctuations in the velocity field which lead to a high level of TKE. Visually, these results are the same as the ones shown in [36].

Fig. 18 compares the second invariant and the TKE along the centerline of the sonar dome vortex, for the IIHR

experiments [45], the EARSM and DDES-SST results from [36], and the current DDES-SST result. The RANS simulation gives a reasonable initial Q but the values drop off too quickly, while the turbulence is underestimated by several orders of magnitude. The original DDES-SST simulation on the other hand has the right tendencies up to $x/L = 0.4$ where the finest refinement box ends. Up to this point, the adapted mesh gives almost the same solution as the fixed mesh. However, it conserves the same tendencies as the experiment everywhere. This is also confirmed by the two cut planes in Fig. 19: the TKE at $x/L = 0.3$ is almost identical on the adapted and the fixed mesh, while the adapted mesh gives good agreement with the experiments at $x/L = 1$.

This indicates that the adapted mesh is suitable for representing the entire flow field and that the physical behavior as shown in Figures 16 and 17 is correct. Thus, the average-based refinement procedure is successful for the simulation of this flow.

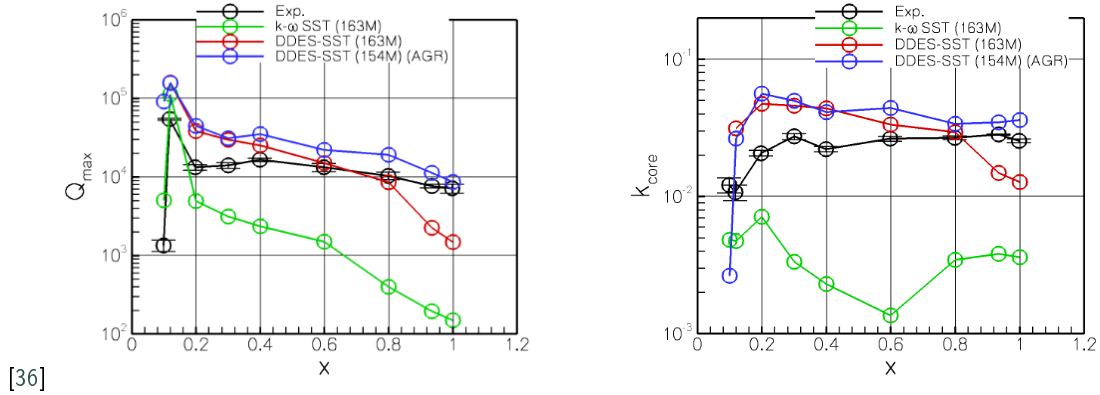


Figure 18: Second invariant Q^* (left) and turbulence kinetic energy k along the center of the sonar dome vortex.

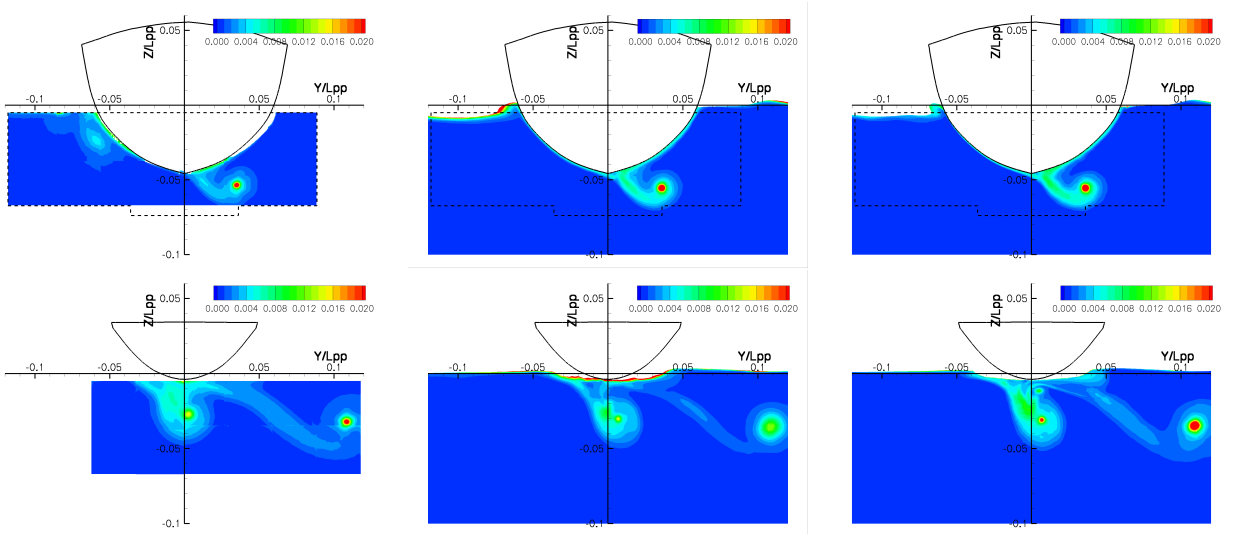


Figure 19: Turbulence kinetic energy for (left to right) experiments, fixed-grid DDES-SST, and adaptive-grid DDES-SST. Top: $x/L = 0.3$, bottom: $x/L = 1$.

Adapted mesh The converged DDES-SST mesh has 154M cells (47M cells for the precursor EARSM simulation). The fine DDES-SST mesh (Fig. 20) follows the sonar dome vortex (right), detects the creation of the windward bilge keel vortex (left-center) and also provides fine cells in the shear layers which connect the vortex cores and the boundary layers. This is different from the 163M fixed fine mesh, where the $\lambda/4$ refinement box only captures the sonar dome

vortex up to $x/L = 0.4$. Finally, refinement around the free surface captures the waves created by the ship. Therefore, the adaptation leads to a more complete solution (Figures 18 and 19) with slightly less cells than the fixed grid. Thanks to the criterion averaging, the mesh is remarkably smooth, with gradual transitions between regions of coarser and finer cells, which improves the accuracy of the discretization.

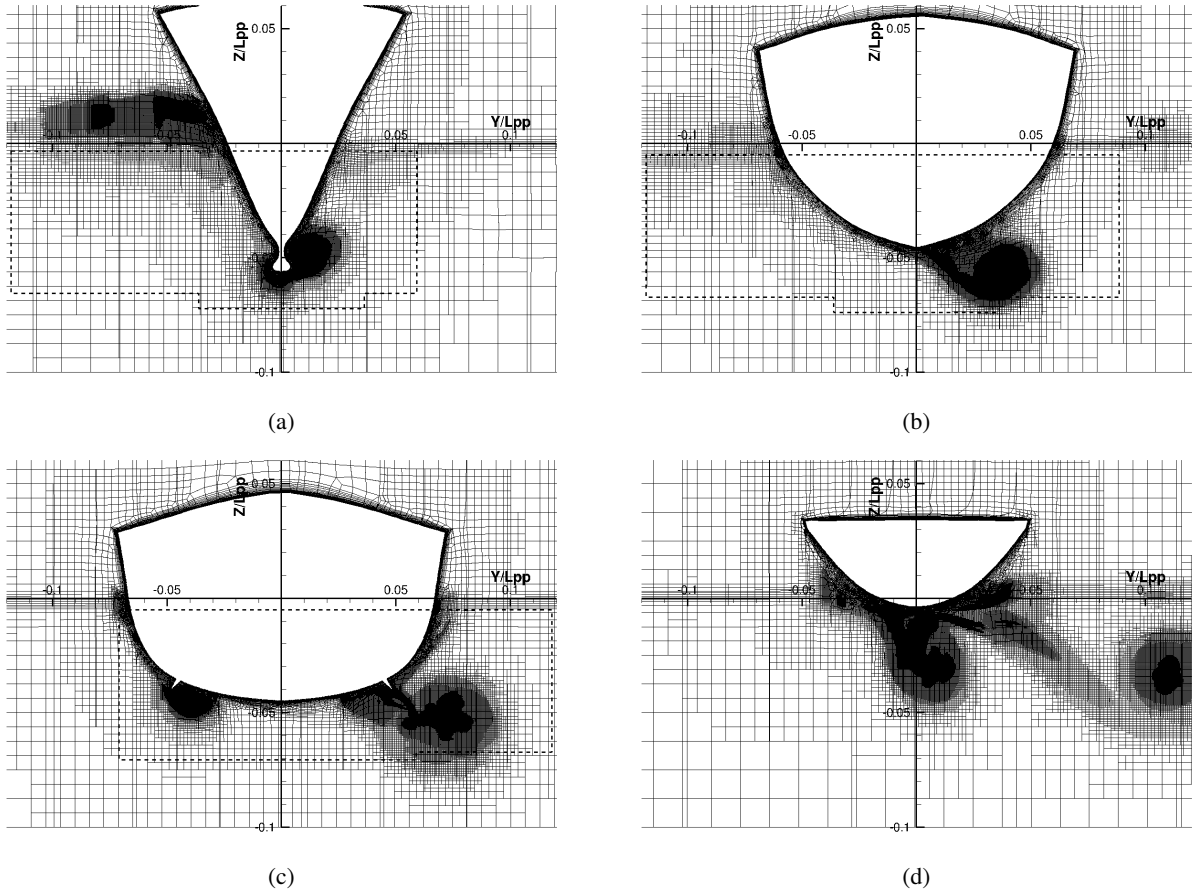


Figure 20: Cross-sections of the adapted mesh. $x/L = 0.1$ (a), $x/L = 0.3$ (b), $x/L = 0.6$ (c) and $x/L = 1.0$ (d).

Fig. 21 presents the mesh in several sections of the sonar dome vortex core. The figure shows how the finest turbulent structures created at the sonar dome gradually evolve into larger vortices. However, the vortex core is resolved everywhere on a mesh with cell size $\lambda_T/4$, thanks to the minimum cell size imposed for the adaptive refinement. As a result, the meshing goal of the average-based refinement is met: the vortex core evolves on a locally uniform mesh which does not evolve in time, nor change in space.

Convergence of the mesh refinement For the flow to converge rapidly to a statistically steady state, a more or less time-independent mesh should be in place as soon as possible. However, the refinement convergence may be slow because the flow and the mesh are linked and converge together: on an insufficiently refined mesh, the flow cannot develop enough, which in turn slows down the mesh refinement.

Here the DDES-SST mesh converges rapidly, thanks to the RANS precursor computation and the short sliding window average (Fig. 22). The RANS mesh converges slowly: the main growth takes about 10 seconds (5 time units or 500 time steps), while the mesh does not fully converge until 25 time units. This is because the initial mesh is not refined at all; the mesh refinement in the vortex cores grows slowly until both the mesh and the vortices reach the back of the ship. The DDES-SST mesh however converges in 3 seconds or 1.5 time units. Since one unit is the time for the flow to pass the length of the ship, this means that the refined mesh is established almost as soon as the first unsteady eddies coming from the sonar dome reach the back of the ship.

Average-based mesh adaptation

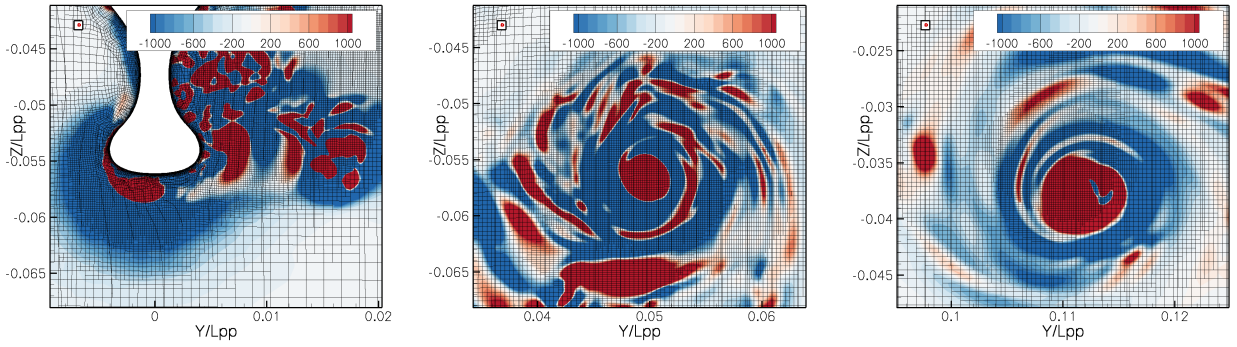


Figure 21: Views of the mesh and the instantaneous Q-criterion in cross-sections across the center of the sonar dome vortex. Left to right: $x/L = 0.1$, $x/L = 0.4$, $x/L = 1$. The black box in the top left corner represents the estimated Taylor microscale, the red box the minimum cell size.

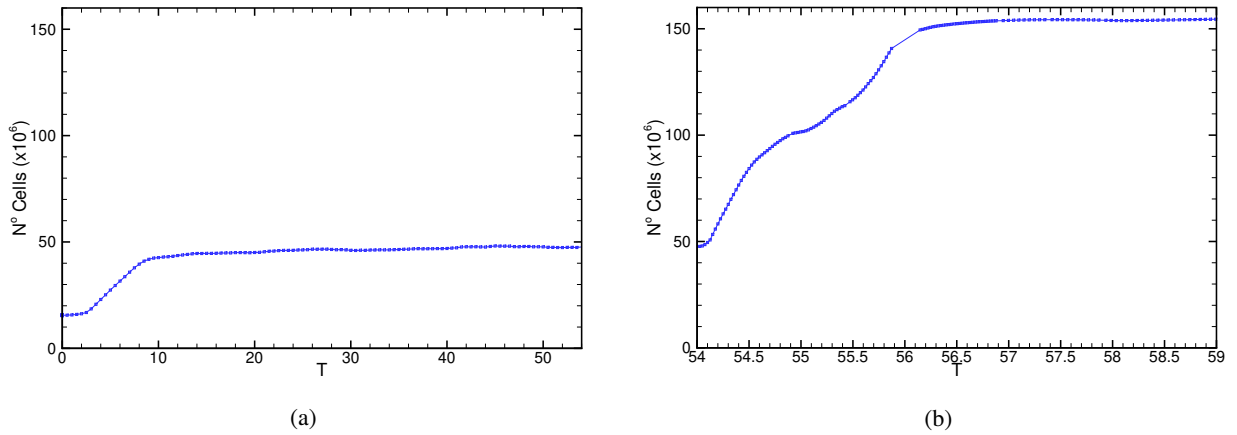


Figure 22: Evolution of the number of cells in the adaptively refined grids of the DTMB 5512, for EARSM (a) and DDES-SST (b) (restarted from the EARSM solution), as a function of the simulation time. The change of averaging interval can be seen around 56s.

Fig. 23, which shows the convergence in two mesh cuts, confirms this. After 0.675 time units in the DDES-SST simulation, the mesh at $x/L = 0.4$ is nearly converged. At $x/L = 0.6$, the sonar dome vortex (whose eddies have to travel $0.6L$ from the front of the sonar dome) is not converged; however, the wake of the leeward bilge keel, which is created closer to $x/L = 0.6$ (see Fig. 16) is almost the same as for the final DDES-SST mesh. Fig. 23 also shows that, while the RANS mesh is coarser than the DDES-SST mesh in the vortex cores, it is fine enough to resolve the largest eddies. Thus, the resolved turbulence can travel rapidly downstream, which causes the fast convergence of the DDES-SST mesh, similar to Section 4.5. Thanks to its large time steps, the RANS precursor computation is efficient for speeding up the convergence of DDES-SST.

5.2. Hybrid delta wing at high angles of attack

In the NATO/AVT-316 project on the simulation of vortex-vortex interaction, the flow around a simplified aircraft geometry with a hybrid delta wing at high angles of incidence is studied. A hybrid delta wing generates several interacting leading edge vortices, whose position is highly dependent on the flow conditions and difficult to predict in advance. This makes the generation of suitable fine meshes difficult.

Therefore, all computations at ECN/CNRS within this project are performed with adaptive meshing, using averaged criteria for the hybrid RANS/LES cases. However, some RANS models predicted unsteady flow at higher angles of attack (incorrectly, since according to the RANS velocity decomposition, with the right Reynolds stresses, the mean flow should be steady). This unsteadiness makes average-based refinement potentially attractive even for RANS. This

Average-based mesh adaptation

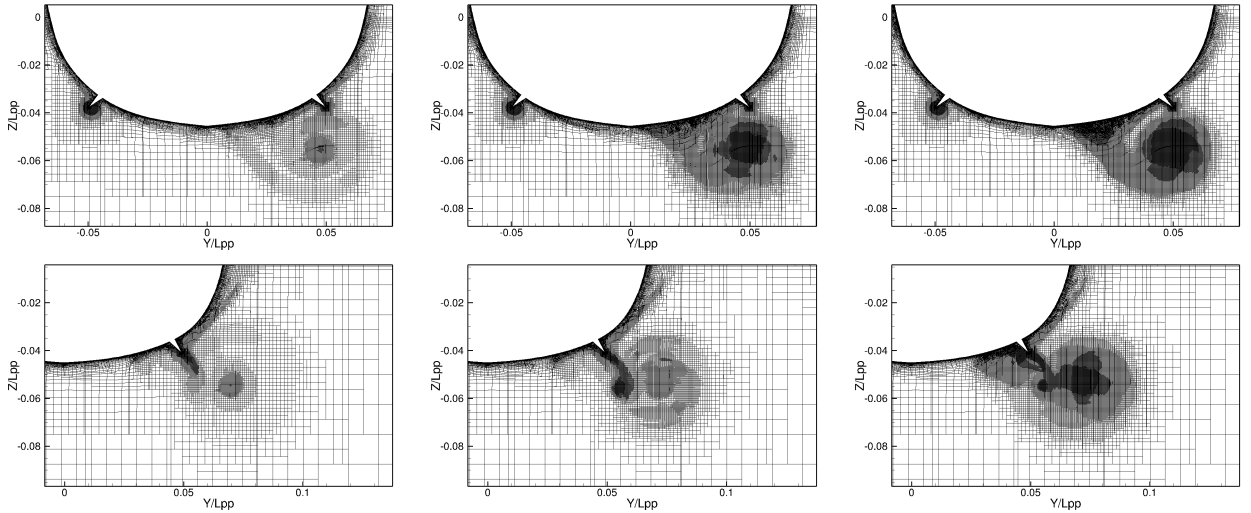


Figure 23: Mesh: left to right, EARSM, DDES (after 0.675 time units), DDES (at the end of the computation). Top: $x/L = 0.4$, bottom: $x/L = 0.6$.

section compares average-based and instantaneous criteria where applicable and shows that the adaptive meshes allow the reliable comparison of different turbulence models.

Test case and flow field The geometry is a simplified fighter jet at model scale (maximum chord $L = 0.8022\text{m}$). Subsonic flow is studied at $V = 51.97\text{m/s}$, $Re = 2.17 \cdot 10^6$ and $M = 0.15$, so incompressible simulation is acceptable. Measurements for this case have been performed at the Technical University of Munich [27]. Simulations are shown with $k - \omega$ SST, with the SSGLRR- ω Reynolds-stress RANS model [5], and with DDES-SST, for an angle of attack $\alpha = 24^\circ$. The initial mesh has a wall-resolved boundary layer with $y^+ < 1$ for the first layer and 15.4M cells in total. The time step is $\Delta t = 1.5 \cdot 10^{-4}\text{s}$ for all the turbulence models.

For the adaptive grid refinement, the instantaneous criterion with threshold $L/5$ is computed every 5 time steps, then averaged (AC) over the entire computation time. To speed up the convergence, the DDES-SST computation is a restart of a $k - \omega$ SST RANS simulation. The minimum cell size for DDES-SST is 1mm, to correspond to the Taylor microscale of $\lambda_T = 2.86\text{mm}$; for RANS, the minimum cell size is 0.5mm. The mesh is adapted every 10 time steps. Converged mesh sizes are 60M ($k - \omega$ SST), 68M (SSGLRR), and 77M (DDES-SST). The CPU times per computation are 30 000 h and 60 000 h, on average, for RANS and DES computations, respectively.

Fig. 24 shows the average and instantaneous DDES-SST flow at $\alpha = 24^\circ$. The main unsteady vortex created on the forward delta wing has a back-flowing core, so there is a shear flow around the core that stimulates the unsteadiness. The vortex created on the leading edge of the second delta wing is moving so much at $\alpha = 24^\circ$, that it is difficult to see in the average flow. Finally, on the top of the hull in front of the wing, a weak and relatively steady vortex is created which moves below the other two vortices.

Refined meshes A cut through the meshes for the three turbulence models is shown in Fig. 25. The steady $k - \omega$ SST solution allows the use of instantaneous refinement criteria, so the mesh refinement reacts to all the details of the flow. As the SSGLRR solution is unsteady, average-based refinement has been used. Thus, the mesh around the vortex cores is smoother than for $k - \omega$ SST, since it is based on all the shear layer positions which occur, while it is less fine in the shear layers due to the criterion averaging. The DDES mesh in Fig. 25c is even smoother and more uniform than the SSGLRR mesh, since it has to resolve eddies which spread out over the entire vortex region (see Fig. 24b). Thus, the average-based refinement reduces the capability to capture very fine details of the flow on an evolving mesh, if the flow is unsteady (for steady flows, instantaneous and average-based refinement are equivalent). Still, the greater smoothness of the average-based meshes has a positive effect on the solution accuracy. Thus, even for RANS flows with some unsteadiness, it makes sense to use average-based refinement.

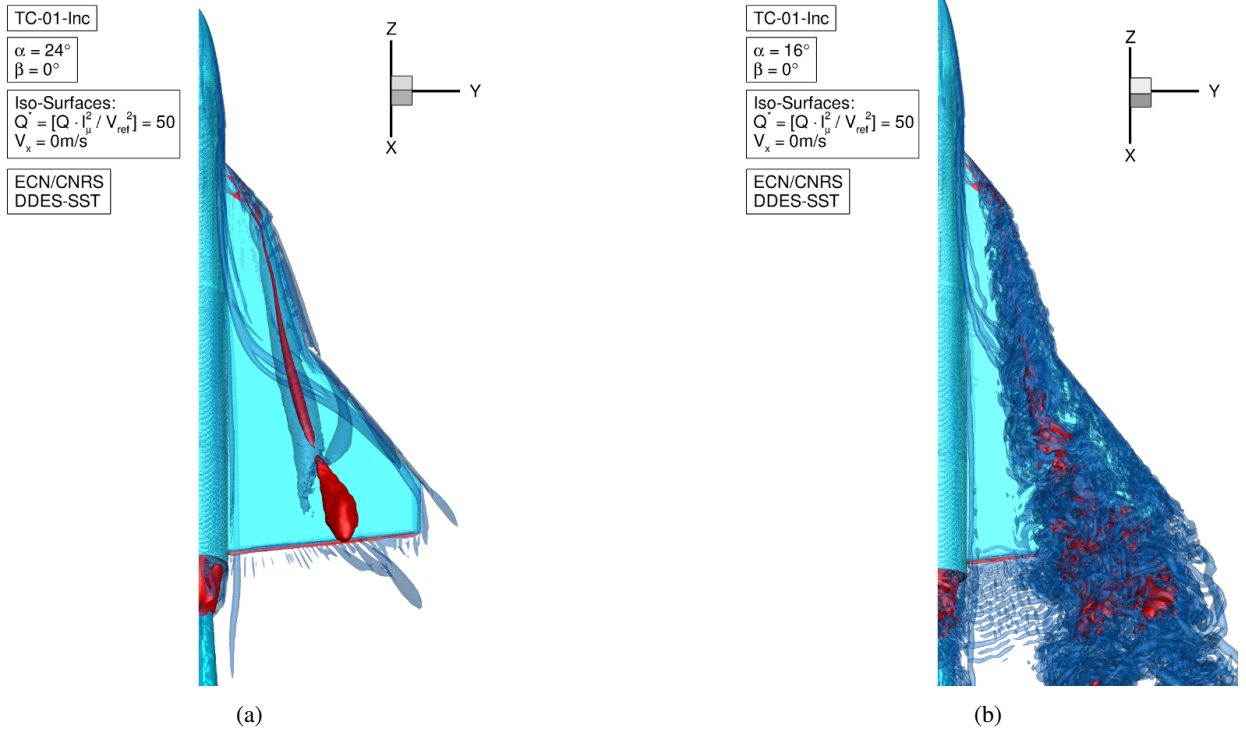


Figure 24: Iso-surfaces of $Q^* = 50$ (blue) and $u < 0$ (red), for DDES-SST. Average (a) and instantaneous (b) flow.

Effect of the turbulence models Since no reference computations on fixed meshes are available, the solutions are compared with each other and with experiments. The experimental results in Fig. 26 show the primary vortex with backflow in its center, accelerated flow on top and a maximum TKE in the shear layer around the back-flowing core. The second vortex has a high-velocity core with maximum TKE in its center. These features are predicted very well by the classic $k - \omega$ SST model. However, the model shows too much thickening of the boundary layer, possibly due to the wing-body vortex. The SSGLRR Reynolds Stress Transport model on the other hand, predicts a smeared-out velocity field with higher TKE than in the experiments, because the vortex is unsteady and moves around. While the exact cause for this is unknown, it is logical that unphysical movement in a RANS solution leads to differences with the experiments. The refined mesh in Fig. 25b is coherent with the flow. Finally, the DDES-SST model produces results that are close to the experiments. Compared with $k - \omega$ SST, there is less thickening of the inboard boundary layer, but more turbulence on the outboard part of the wing. The strength of the velocity peaks in the vortex cores is slightly overestimated and the predicted TKE in the first vortex is too high, with a maximum in the center instead of on the shear layer. This small overestimation is coherent with the results for the DTMB 5512.

Fig. 27 shows the evolution of the global forces and moments with α . The results are coherent with the observations at $\alpha = 24^\circ$: both $k - \omega$ SST and DDES-SST predict the evolution of the forces well, while SSGLRR gives good results at lower angles of attack but is less accurate at $\alpha = 24^\circ$. Thus, both the global and the local results agree well with experiments. The average-based refinement for DDES-SST and the instantaneous refinement for $k - \omega$ SST give very similar results and the meshes correspond visually to what would be expected. These are all indications that the average-based refinement is successful.

6. Conclusion

This paper studies the feasibility of using adaptive grid refinement (AGR) to create the meshes for the simulation of complex flows with hybrid RANS/LES turbulence models. A complication is that these turbulence models are very sensitive to the mesh size, as well as its variations in time and space. For example, the local mesh resolution has an effect on the turbulence production and decay rate. Moreover, due to the strong spatial variation of the solution, interpolations between coarse and fine meshes are prone to errors. Finally, a loss of resolved TKE occurs at interfaces

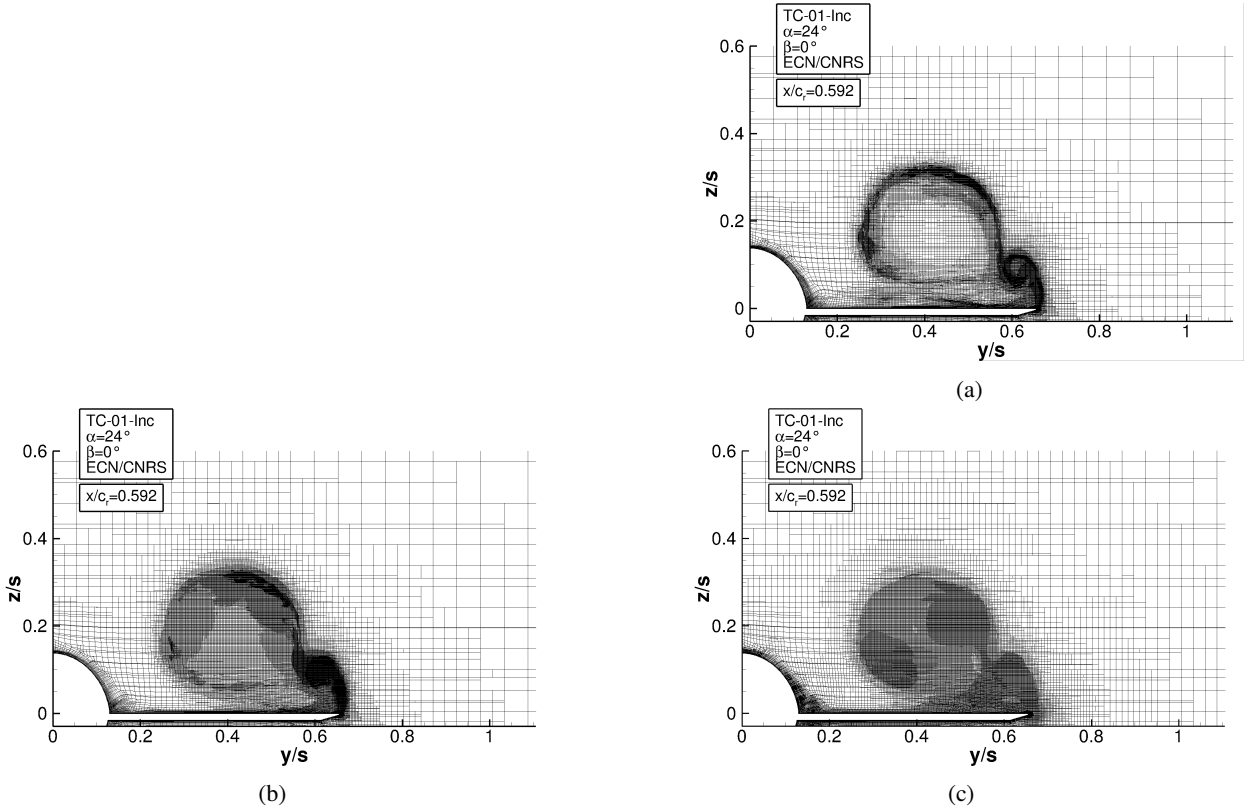


Figure 25: Adapted meshes at $x/L = 0.592$, for $k-\omega$ SST (a), SSGLRR (b), and DDES-SST (c).

between fine and coarse cells and also, by extension, when the mesh changes in time. When standard AGR is used for hybrid RANS/LES simulations, such mesh variations are inevitable since, due to the local and extreme fluctuations in the velocity, many spatial and temporal changes are imposed on the mesh by the adaptation.

The approach proposed here, on the contrary, uses adaptive mesh refinement to reduce as much as possible the temporal and spatial variations which the main flow features encounter. For statistically steady flows, this requires meshes which are close to uniform in size along the path of the different flow elements. For complex flows, where the flow behavior is impossible to predict before a simulation, AGR is an ideal tool to achieve such meshes.

Average-based refinement Quasi-steady adapted meshes are obtained here by basing the refinement criterion (which dictates where the mesh is refined) on time-averaged quantities. Since there are many different ways to implement such an approach, a first test of a backward-facing step flow was used to analyze these options and to provide guidelines for the right choices. The tests reveal that the average-based adaptation is most effective when the averaging process is applied over the instantaneous refinement criteria. This makes sense because the mesh must be suitable, in an averaged sense, for the instantaneous flow at all times. The alternative of computing the refinement criterion from the averaged flow is attractive in terms of computational cost and memory, but inefficient if the average flow does not resemble the instantaneous flows.

Two time windows are considered for applying the averaging process: the entire-simulation averaging which averages over all the preceding instantaneous refinement criteria and the sliding window averaging which is applied only over the criteria of a specific number of previous time steps. Reducing the length of the averaging interval creates a refinement criterion which reacts more to the dynamics of the flow, which leads to more mesh changes. By selecting a proper averaging interval, high-frequency flow instabilities are represented in an average sense, while the main unsteady behavior of the flow is preserved in the time-evolution of the average solution. Also, a short window can help in eliminating the initial transients from the criterion and can lead to faster convergence of the mesh for statistically steady flows. Selecting the optimal averaging interval is case dependent and the physics of the flow must be considered; to

Average-based mesh adaptation

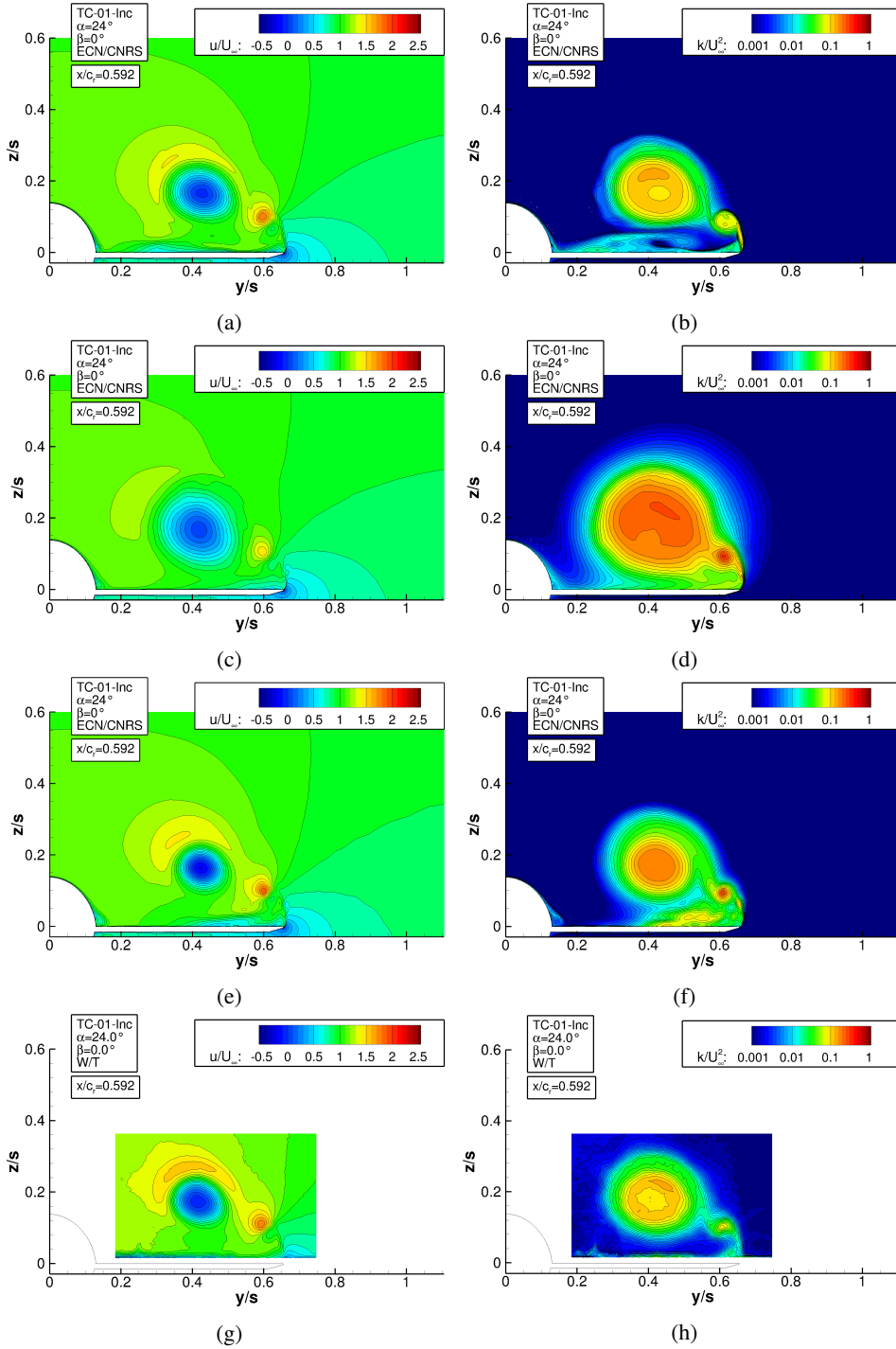


Figure 26: Axial velocity (a,c,e,g) and turbulence kinetic energy (b,d,f,h) at $x/L = 0.592$, for the experiments (g/h), $k-\omega$ SST (a/b), SSGLRR (c/d), and DDES-SST (averaged flow) (e/f).

average out a physical phenomenon, the window should span at least 4 to 10 of its characteristic periods.

For the BFS flow, reducing the refinement threshold to produce a globally finer mesh, results in more accurate solutions compared to the experimental results. This grid convergence shows the well-foundedness of the refinement approach. Furthermore, adding initial refinement boxes in either the full recirculation zone or the shear layer

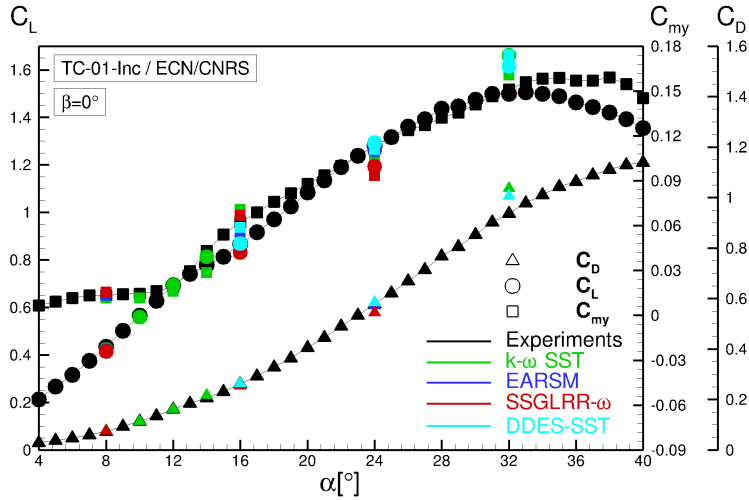


Figure 27: Force and moment coefficients as a function of the angle of attack, for the hybrid delta wing.

only, accelerates the convergence and leads to similar refined meshes. The grid convergence and refinement box test demonstrate that the second-derivative based refinement criterion, which refines the mesh only in zones of strong flow activity, is suitable even for hybrid RANS/LES simulations. Also, the tests show that a sufficiently fine initial grid can accelerate the convergence of the mesh adaptation in time.

Realistic flows The paper then evaluates adaptive grid refinement for hybrid RANS/LES simulation of two challenging flows with longitudinal vorticity, using the lessons learned from the BFS case. Refinement based on the average of the instantaneous criteria is used. To obtain a converged mesh rapidly, a fine initial grid is obtained by starting from a converged RANS simulation, whose mesh is already refined around the main flow features. Furthermore, the criterion for the DTMB 5512 is averaged over a (short) sliding window. To obtain a stable final mesh, this is switched to an average over the entire computation time once the mesh starts to converge, which occurs in less than 1.5 flow passage times. The turbulence in the main flow features is best preserved on meshes which are locally uniform in size; these are obtained by imposing a cutoff cell size for the refinement. A minimum cell size of $\frac{1}{4}$ the Taylor microscale is adequate. All hybrid LES simulations are run with the same thresholds as the corresponding RANS simulations, which lie between $L/5$ and $L/20$. If these produce an adequate RANS mesh, then the same settings applied to DDES-SST also provide a good mesh for the hybrid turbulence simulation.

The results for the DTMB 5512 show that the same flow behavior is obtained on an adapted mesh as on a fixed fine mesh and that, with a similar number of cells, a larger part of the flow is resolved correctly. For the hybrid delta wing, consistent results are obtained between average-based and instantaneous refinement criteria. Both the $k-\omega$ SST and DDES-SST results correspond well with the experiments.

Thus, the average-based adaptive refinement can produce reliable simulation results for realistic flows. With respect to the manual creation of locally refined meshes, the grid generation is simplified and computational expenses are reduced because iterative creation of the mesh is no longer needed. The method has therefore proven its worth as a tool for the investigation of complex flow physics.

Acknowledgement

This work was granted access to the HPC resources of CINES/IDRIS under the allocation A0062A0129 made by GENCI (Grand Equipement National de Calcul Intensif), which is gratefully acknowledged. The help of Dr. Hyunse Yoon and Prof. Frederick Stern from IIHR who provided us with the remarkable experiments for the DTMB 5512 at an early stage of this work, as well as TU Munich / Airbus Defense & Space who graciously provided the hybrid delta wing experiments, is warmly acknowledged.

References

- [1] Antepará, O., Lehmkuhl, O., Borrell, R., Chiva, J., Oliva, A., 2015. Parallel adaptive mesh refinement for large-eddy simulations of turbulent flows. *Computers & Fluids* 110, 48–61. doi:10.1016/j.compfluid.2014.09.050.
- [2] Balan, A., Park, M.A., Anderson, W.K., Kamenetskiy, D.S., Krakos, J.A., Michal, T., Alauzet, F., 2020a. Verification of anisotropic mesh adaptation for turbulent simulations over ONERA M6 wing. *AIAA Journal* 58, 1550–1565. doi:10.2514/1.J059158.
- [3] Balan, A., Park, M.A., Wood, S., Anderson, W.K., 2020b. Verification of anisotropic mesh adaptation for complex aerospace applications. doi:10.2514/6.2020-0675.
- [4] Benard, P., Balarac, G., Moureau, V., Dobrzynski, C., Lartigue, G., d'Angelo, Y., 2016. Mesh adaptation for large-eddy simulations in complex geometries. *International journal for numerical methods in fluids* 81, 719–740. doi:10.1002/flid.4204.
- [5] Cécora, R.D., Radespiel, R., Eisfeld, B., Probst, A., 2015. Differential Reynolds-stress modeling for aeronautics. *AIAA Journal* 53, 739–755. doi:10.2514/1.J053250.
- [6] Daviller, G., Brebion, M., Xavier, P., Staffelbach, G., Müller, J.D., Poinot, T., 2017. A mesh adaptation strategy to predict pressure losses in LES of swirled flows. *Flow, Turbulence and Combustion* 99, 93–118. doi:10.1007/s10494-017-9808-z.
- [7] Deng, G.B., Visonneau, M., 1999. Comparison of explicit algebraic stress models and second-order turbulence closures for steady flows around ships, in: 7th Int. Conf. on Numerical Ship Hydrodynamics, Nantes, France.
- [8] Duvigneau, R., Visonneau, M., Deng, G.B., 2003. On the role played by turbulence closures in hull shape optimization at model and full scale. *Journal of Marine Science and Technology* 8, 11–25. doi:10.1007/s10773-003-0153-8.
- [9] Frazza, L., Loseille, A., Alauzet, F., 2019. Unstructured anisotropic mesh adaptation for 3D RANS turbomachinery applications. doi:10.2514/6.2019-3059.
- [10] Gao, X., Groth, C.P., 2010. A parallel solution-adaptive method for three-dimensional turbulent non-premixed combustions flows. *Journal of Computational Physics* 229, 3250–3275. doi:10.1016/j.jcp.2010.01.001.
- [11] George, P.L., Borouchaki, H., 1998. *Delaunay Triangulation and Meshing - Application to Finite Elements*. Hermes, Paris.
- [12] Goodfriend, E., Chow, F., Vanella, M., Balaras, E., 2013. Large-eddy simulation of decaying isotropic turbulence across a grid refinement interface using explicit filtering and reconstruction. *Journal of Turbulence* 14, 58–76. doi:10.1080/14685248.2013.867964.
- [13] Gou, J., Su, X., Yuan, X., 2018. Adaptive mesh refinement method-based large eddy simulation for the flow over circular cylinder at $Re_D=3900$. *International Journal of Computational Fluid Dynamics* 32, 1–18. doi:10.1080/10618562.2018.1461845.
- [14] Gritskevich, M.S., Garbaruk, A.V., Menter, F.R., 2013. Fine-tuning of DDES and IDDES formulations to the $k-\omega$ Shear Stress Transport model. *Progress in Flight Physics* 5, 23–42. doi:10.1051/eucass/201305023.
- [15] Gritskevich, M.S., Garbaruk, A.V., Schütze, J., Menter, F.R., 2012. Development of DDES and IDDES formulations for the $k-\omega$ Shear Stress Transport model. *Flow, Turbulence and Combustion* 88, 431–449. doi:10.1007/s10494-011-9378-4.
- [16] Guilmineau, E., Deng, G., Leroyer, A., Queutey, P., Visonneau, M., Wackers, J., 2018. Assessment of hybrid RANS-LES formulations for flow simulation around the Ahmed body. *Computers & Fluids* 176, 302–319. doi:10.1016/j.compfluid.2017.01.005.
- [17] Hasan, M., 1992. The flow over a backward-facing step under controlled perturbation: laminar separation. *Journal of Fluid Mechanics* 238, 73–96. doi:10.1017/S0022112092001642.
- [18] Hu, R., Wang, L., Fu, S., 2016. Investigation of the coherent structures in flow behind a backward-facing step. *International Journal of Numerical Methods for Heat & Fluid Flow* 26, 1050–1068. doi:10.1108/HFF-09-2015-0403.
- [19] Kamkar, S., Wissink, A.M., Sankaran, V., Jameson, A., 2011. Feature-driven Cartesian adaptive mesh refinement for vortex-dominated flows. *Journal of Computational Physics* 230, 6271–6298. doi:10.1016/j.jcp.2011.04.024.
- [20] Leonard, B.P., 1991. The ULTIMATE conservative difference scheme applied to unsteady one-dimensional advection. *Computer Methods in Applied Mechanics and Engineering* 88, 17–74. doi:10.1016/0045-7825(91)90232-U.
- [21] Limare, A., Borouchaki, H., Brenner, P., 2020. Adaptive mesh refinement with an automatic hybrid RANS/LES strategy and overset grids, in: *Progress in Hybrid RANS-LES Modelling*. Springer, pp. 159–168. doi:10.1007/978-3-030-27607-2_12.
- [22] Loseille, A., Dervieux, A., Alauzet, F., 2010. Fully anisotropic goal-oriented mesh adaptation for 3D steady Euler equations. *Journal of Computational Physics* 229, 2866–2897. doi:10.1016/j.jcp.2009.12.021.
- [23] Mozaffari, S., 2020. *Adaptive Grid Refinement for Hybrid RANS/LES*. Ph.D. thesis. École Centrale de Nantes.
- [24] Mozaffari, S., Visonneau, M., Wackers, J., 2020. Average-based adaptive grid refinement in hybrid LES, in: *Direct and Large Eddy Simulation XII*, Springer International Publishing, Cham. pp. 449–455. doi:10.1007/978-3-030-42822-8_59.
- [25] Naddei, F., de la Llave Plata, M., Couaillier, V., Coquel, F., 2019. A comparison of refinement indicators for p-adaptive simulations of steady and unsteady flows using discontinuous Galerkin methods. *Journal of Computational Physics* 376, 508–533. doi:10.1016/j.jcp.2018.09.045.
- [26] Park, M.A., Kleb, W.L., Anderson, W.K., Wood, S.L., Balan, A., Zhou, B.Y., Gauger, N.R., 2020. Exploring unstructured mesh adaptation for Hybrid Reynolds-Averaged Navier–Stokes/Large Eddy Simulation, in: *AIAA SciTech 2020 Forum*, pp. 11–39. doi:10.2514/6.2020-1139.
- [27] Pfnür, S., Breitsamter, C., 2019. Leading-edge vortex interactions at a generic multiple swept-wing aircraft configuration. *Journal of Aircraft* 56, 2093–2107. doi:10.2514/1.C035491.
- [28] Piomelli, U., Kang, S., Ham, F., Iaccarino, G., 2006. Effect of discontinuous filter width in large-eddy simulations of plane channel flow. *Studying turbulence using numerical databases XI*, 151–162.
- [29] Queutey, P., Visonneau, M., 2007. An interface capturing method for free-surface hydrodynamic flows. *Computers & Fluids* 36, 1481–1510. doi:10.1016/j.compfluid.2006.11.007.
- [30] Sagaut, P., Deck, S., Terracol, M., 2013. *Multiscale and Multiresolution Approaches in Turbulence*. 2nd ed., Imperial College Press. doi:10.1142/p878.
- [31] Shur, M.L., Spalart, P.R., Strelets, M.K., 2016. Jet noise computation based on enhanced DES formulations accelerating the RANS-to-LES transition in free shear layers. *International Journal of Aeroacoustics* 15, 595–613. doi:10.1177/1475472X16659388.
- [32] Shur, M.L., Spalart, P.R., Strelets, M.K., Travin, A.K., 2008. A hybrid RANS-LES approach with delayed-DES and wall-modelled LES

- capabilities. *International Journal of Heat and Fluid Flow* 29, 1638–1649. doi:10.1016/j.ijheatfluidflow.2008.07.001.
- [33] Spalart, P.R., Deck, S., Shur, M.L., Squires, K.D., Strelets, M.K., Travin, A.K., 2006. A new version of detached-eddy simulation, resistant to ambiguous grid densities. *Theoretical and Computational Fluid Dynamics* 20, 181–195. doi:10.1007/s00162-006-0015-0.
- [34] Toosi, S., Larsson, J., 2017. Anisotropic grid-adaptation in large eddy simulations. *Computers & Fluids* 156, 146–161. doi:10.1016/j.compfluid.2017.07.006.
- [35] Turnow, J., Kasper, R., Kornev, N., 2018. Flow structures and heat transfer over a single dimple using hybrid URANS-LES methods. *Computers & Fluids* 172, 720–727. doi:10.1016/j.compfluid.2018.01.014.
- [36] Visonneau, M., Guilmineau, E., Rubino, G., 2018. Computational analysis of the flow around a surface combatant at 10° static drift and dynamic sway conditions, in: 32nd Symposium on Naval Hydrodynamics, Hamburg, Germany.
- [37] Visonneau, M., Guilmineau, E., Rubino, G., 2020. Local flow around a surface combatant at various static drift conditions: The role played by turbulence closures, in: 33rd Symposium on Naval Hydrodynamics, Osaka, Japan.
- [38] Vivarelli, G., Qin, N., Shahpar, S., Radford, D., 2018. Efficient adjoint-based mesh adaptation applied to turbo-machinery flows, in: Turbo Expo: Power for Land, Sea, and Air, American Society of Mechanical Engineers. doi:10.1115/GT2018-77066.
- [39] Vogel, J., Eaton, J.K., 1985. Combined heat transfer and fluid dynamic measurements downstream of a backward-facing step. *Journal of Heat Transfer* 107, 922–929. doi:10.1115/1.3247522.
- [40] Wackers, J., Ait Said, K., Deng, G.B., Queutey, P., Visonneau, M., Mizine, I., 2010. Adaptive grid refinement applied to RANS ship flow computation, in: 28th Symposium on Naval Hydrodynamics, Pasadena, California.
- [41] Wackers, J., Deng, G., Guilmineau, E., Leroyer, A., Queutey, P., Visonneau, M., 2014. Combined refinement criteria for anisotropic grid refinement in free-surface flow simulation. *Computers & Fluids* 92, 209–222. doi:10.1016/j.compfluid.2013.12.019.
- [42] Wackers, J., Deng, G.B., Guilmineau, E., Leroyer, A., Queutey, P., Visonneau, M., Palmieri, A., Liverani, A., 2017. Can adaptive grid refinement produce grid-independent solutions for incompressible flows? *Journal of Computational Physics* 344, 364–380. doi:10.1016/j.jcp.2017.04.077.
- [43] Wackers, J., Deng, G.B., Leroyer, A., Queutey, P., Visonneau, M., 2012. Adaptive grid refinement for hydrodynamic flows. *Computers & Fluids* 55, 85–100. doi:10.1016/j.compfluid.2011.11.004.
- [44] Wackers, J., Koren, B., Raven, H.C., Van der Ploeg, A., Starke, A., Deng, G., Queutey, P., Visonneau, M., Hino, T., Ohashi, K., 2011. Free-surface viscous flow solution methods for ship hydrodynamics. *Archives of Computational Methods in Engineering* 18, 1–41. doi:10.1007/s11831-011-9059-4.
- [45] Yoon, H., Gui, L., Bhushan, S., F., S., 2014. Tomographic PIV measurements for a surface combatant at straight ahead and static drift conditions, in: 30th Symposium on Naval Hydrodynamics, Hobart, Tasmania, Australia.
- [46] Zhou, B.Y., Diskin, B., Gauger, N.R., Pardue, J.K., Chernikov, A., Tsolakis, C., Drakopoulos, F., Chrisochoides, N.N., 2019. Hybrid RANS/LES simulation of vortex breakdown over a delta wing, in: AIAA Aviation 2019 Forum, p. 3524. doi:10.2514/6.2019-3524.